Available online at www.sciencedirect.com

SCIENCE DIRECT®

Earth and Planetary Science Letters 227 (2004) 457–472

EPSL

www.elsevier.com/locate/epsl

Fractionation of noble gases (He, Ar) during MORB mantle melting: a case study on the Southeast Indian Ridge

Pete Burnard[a,*], David Graham[b], Ken Farley[a]

[a]*Division of Geological and Planetary Sciences, California Institute of Technology MS100-23, Pasadena CA91125, USA*
[b]*College of Oceanic and Atmospheric Sciences, Oregon State University, Corvallis, OR97331-5503, USA*

Received 21 January 2004; received in revised form 22 April 2004; accepted 18 August 2004
Available online 13 October 2004
Editor: B. Wood

Abstract

New measurements of the He, Ar and CO_2 abundances trapped in basaltic glasses from the Southeast Indian Ridge (SEIR) show that volatile concentrations in the SEIR magmas were controlled by fractional degassing. Fractionation between volatile species is consistent with their solubilities in silicate melts. As a result, there are linear relationships between (for example) $\ln(^4He/^{40}Ar^*)$ vs. $\ln[^{40}Ar^*]$ and between $\ln(^4He/^{40}Ar^*)$ vs. $\ln(^{40}Ar^*/CO_2)$ (where $^{40}Ar^*$ is the ^{40}Ar corrected for atmospheric contributions). The slopes of these correlations permit the relative He/Ar and Ar/CO_2 solubilities to be estimated; these are generally consistent with experimentally determined noble gas solubilities in basaltic melts.

However, there are systematic differences in the degassing trajectories. For example, in a plot of $\ln(^4He/^{40}Ar^*)$ vs. $\ln(^{40}Ar^*/CO_2)$, samples from the deepest portions of the ridge consistently plot at lower $^4He/^{40}Ar^*$ for a given $^{40}Ar^*/CO_2$, compared to shallower sections of ridge. These variations in $^4He/^{40}Ar^*$ likely reflect variations in He/Ar in the primary melt, i.e. their relative abundances prior to degassing. We estimated the variation in $^4He/^{40}Ar^*$ in the initial melts (i.e. the $^4He/^{40}Ar^*$ prior to degassing) by extrapolating the degassing trend to a constant mantle-like $^{40}Ar^*/CO_2$ ratio and assuming that the relative He–Ar–CO_2 solubilities do not vary between samples. The $^4He/^{40}Ar^*$ corrected for degassing in this manner varies by a factor ≈ 10 and correlates positively with the $^3He/^4He$ ratio.

It is possible that the correlation between "degassing corrected" $^4He/^{40}Ar^*$ ratios and the $^3He/^4He$ ratio results from preferential diffusion of ^3He relative to ^4He and of ^4He relative to ^{40}Ar from the solid mantle into primary melts during melting. However, modeling this diffusive process fails to reproduce the comparatively large variations in $^3He/^4He$ found in the basalts; therefore, it seems likely that mantle heterogeneities, in combination with diffusive fractionation, resulted in coupled He isotope and He/Ar variations.

Keywords: noble gas; degassing; diffusion; mid-ocean ridge basalt; Southeast Indian Ridge; mantle melting

* Corresponding author. now at: Centre de Recherches Pétrographiques et Géochimiques (CRPG-CNRS), 15 rue Notre Dame des Pauvres, B.P. 20, 54501 VANDOEUVRE-les-NANCY Cedex, France. Tel.: +33 38359 4213; fax: +33 38351 1798.
E-mail address: peteb@crpg.cnrs-nancy.fr (P. Burnard).

0012-821X/$ - see front matter © 2004 Elsevier B.V. All rigths reserved.
doi:10.1016/j.epsl.2004.08.021

1. Introduction

The noble gases He, Ne and Ar are highly incompatible elements, which will be preferentially incorporated into a melt during melting of the mantle [1–3], so at partial melt fractions relevant to mid-ocean ridges a primary melt will inherit the relative noble gas abundance pattern of the mantle source. Given that the range of $^4He/^{40}Ar$ ratios of the mantle is likely to vary within narrow and comparatively well-established limits owing to the similar geochemistry of the parents, K, U and Th, the $^4He/^{40}Ar$ ratios of primary melts should also be relatively restricted.

Relative noble gas fractionation is expected to occur during subsequent magmatic degassing as the melts ascend through the crust. During magmatic degassing, $^4He/^{40}Ar^*$ of residual volatiles increases because He is more soluble than Ar (where $^{40}Ar^*=^{40}Ar$ corrected for atmospheric contamination). However, MORBs with the highest $^4He/^{40}Ar^*$ ratios (i.e. those that appear to be most degassed) also have high He concentrations [4,5]. Therefore, He–Ar systematics in oceanic basalts cannot be explained by magmatic degassing alone, but require that there is a variation in the primary melt $^4He/^{40}Ar^*$ [4–6]. Burnard [6] and Matsuda and Marty [4] suggested that preferential diffusion of He (relative to Ar) out of solid mantle during melting could preferentially enrich He relative to Ar in the primary melt. In this scenario, more He than Ar diffuses into the melt, producing a melt where He concentration increases with increasing $^4He/^{40}Ar^*$, as in most MORBs. A direct prediction of this model is that the He/Ar ratio will increase with decreasing partial melt fraction because the ratio (grain surface area)/(melt volume) is maximized during low degrees of partial melting.

An ideal location for testing geochemical responses to variations in melting regime is the Southeast Indian Ridge (SEIR). The progressive increase in average axial depth of the SEIR between 86 °E (slightly east of the Amsterdam–St. Paul (ASP) Plateau) and 118 °E (the western end of the Australian–Antarctic Discordance (AAD)) reflects a progressive decrease in mantle temperature [7] with a predicted decrease in the pressure of the solidus and therefore a lower extent of melting [8,9]. This is reflected in the progressive decrease in Fe_8 and increase in Na_8 compositions eastward along the ridge [10,11], because the Fe content of primary melts decreases with decreasing pressure of melting while the Na content of the melt increases with lower partial melt fraction [12]. If kinetic fractionation of He and Ar occurs during melting, then the extent of fractionation should increase as the partial melt fraction decreases approaching the AAD.

The noble gases (He, Ne, Ar) and CO_2 trapped in vesicles in 29 basaltic glasses from this section of the SEIR were analyzed, with up to 7 repeat analyses of each sample, in order to investigate if the effect (if any) of the melting regime on relative noble gas abundances in MORB lavas could be distinguished from the expected degassing fractionations. We show below how the He–Ar–CO_2 compositions can be used to correct for the degassing process in order to estimate the "pre-degassing" relative He–Ar abundances. The "pre-degassing" relative He–Ar abundances estimated this way vary systematically with the changes in melting regime and correlate with the $^3He/^4He$ ratio of the trapped He. Plausible geological scenarios for these variations are discussed.

1.1. Introduction: degassing

The He–Ar system is an excellent tool with which to study magmatic degassing due to the large difference in He and Ar solubilities, but also because ^4He and $^{40}Ar^*$ are produced by radioactive decay of U+Th and K in the mantle. Therefore, it is possible to model the relative $^4He/^{40}Ar^*$ production ratio of the mantle. Most estimates of the mantle (U+Th)/K ratio (K/U weight ratio of $\approx 1\times10^{-4}$) suggest that the mantle has a $^4He/^{40}Ar^*$ ratio of between 2 and 4 [13,14].

Virtually all oceanic basalts are supersaturated with respect to CO_2 when they erupt, resulting in two-phase magmas consisting of bubbles of volatiles and a silicate liquid [15]. The noble gases partition between the two phases according to Henry's law, after which the bubbles remain isolated from the gases remaining in the melt: variable He–Ar–CO_2 concentrations within individual sub-samples of basaltic glass [16–18] demonstrate that the bubbles do not immediately re-equilibrate with the surrounding magma. Thus, formation of bubbles will fractionate the relative abundances of noble gases in basaltic glasses. Noble gas solubilities increase with decreasing mass such that He is the most soluble; experimental work suggests

that the relative He/Ar solubilities in MORBs are in the range 7–10, varying within this range as a function of melt composition [19,20] and volatile (CO_2 and H_2O) concentrations [21,22]. Work by Marty and Zimmerman [23], Moreira and Sarda [24], Sarda and Moreira [25], Burnard [18,26] and Burnard et al. [27,28] show that there is good agreement between experimentally determined solubilities and the effective relative solubilities during natural degassing of basaltic magmas: decreasing $^{40}Ar^*$ concentrations with increasing $^4He/^{40}Ar^*$ in basaltic glasses can be modeled by either a Rayleigh (fractional) degassing process, or a combination of batch degassing with mixing between the fractionated bubble compositions and less fractionated melt [25]. Note that He concentrations in basalts are poor tracers of degassing as He is the most soluble noble gas; as demonstrated by [25,27], Ar concentrations show larger variations and are negatively correlated with $^4He/^{40}Ar^*$ ratios, as would be expected for a degassing magma.

The concentrations of volatiles—noble gases and CO_2—in oceanic basaltic glasses therefore depend on the extent of gas loss from the magma and on the efficiency that vesicles are nucleated and preserved in the glass (Fig. 1). It is easy to envisage a situation in which a "control volume" of magma experiences vesicle depletion, and hence a decrease in volatile concentrations, during "sweeping" by a large vesicle (which will ascend more rapidly, entraining vesicles and leaving a bubble-free region of magma in its wake [29]), or simply by vertical ascent of the vesicles through the magmatic system.

2. Samples and geological background

The samples used in this study were dredged by the RV Melville in 1996 on the Westward10 expedition to the SEIR: a summary of their locations is given in Table 1 (Supplementary Information) and shown in Fig. 2. The chemistry and isotopic compositions of the basalts have been reported by Mahoney et al. [10], while vesicle He concentrations and isotopic compositions of the WW10 samples were reported by Graham et al. [11].

All samples analyzed here were dredged from, or very close to, the active spreading axis (Fig. 2). These samples cover a range in compositions from normal,

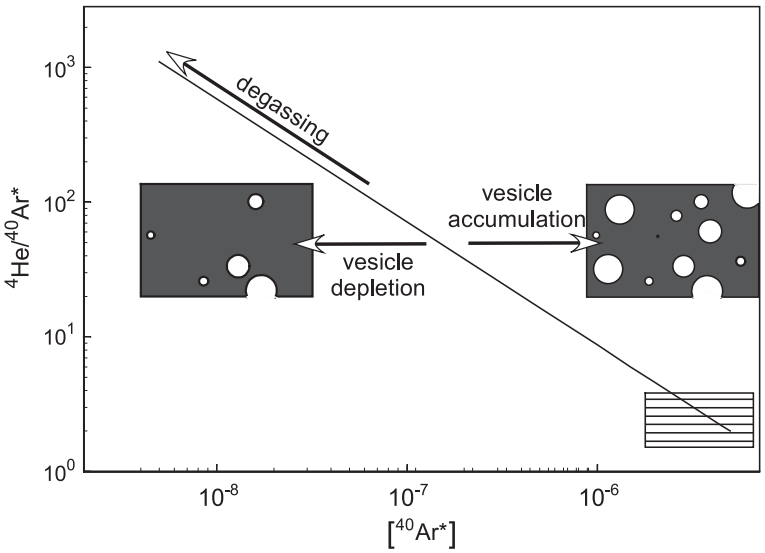

Fig. 1. Effects of degassing on noble gas concentrations and $^4He/^{40}Ar^*$ ratios. Degassing will reduce $^{40}Ar^*$ concentrations while increasing $^4He/^{40}Ar^*$; assuming that the process is dominantly fractional with relative He/Ar solubilities similar to experimentally determined values, there should be an inverse relationship between $\ln(^4He/^{40}Ar^*)$ and $\ln([^{40}Ar^*])$ in the residual volatiles, as shown in the figure. The mantle $^4He/^{40}Ar^*$ is likely in the range 2–4 but the initial $[^{40}Ar^*]$ concentration is not well constrained. However, noble gases in basaltic glasses are predominantly trapped in vesicles; consequently, the distribution of vesicles will also affect the measured $^{40}Ar^*$ concentrations without significantly affecting the $^4He/^{40}Ar^*$.

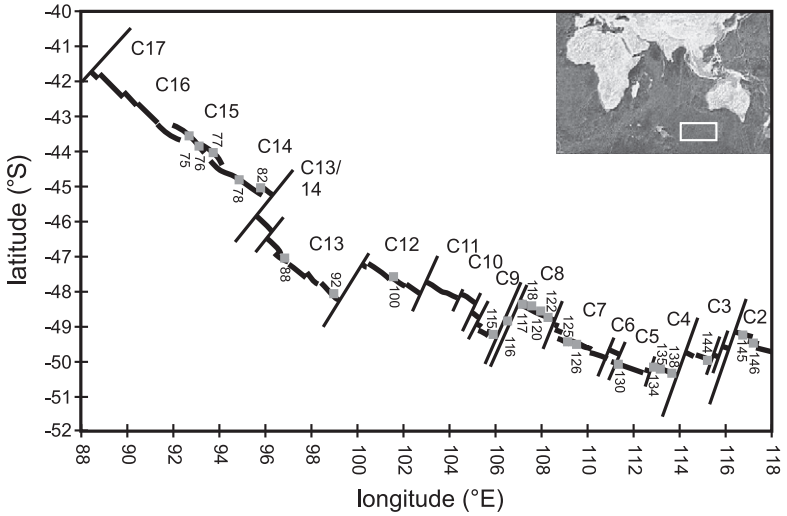

Fig. 2. Map of the Southeast Indian Ridge showing major segmentation and segment numbers (C17. . .C2). Location of dredges from which samples were analyzed during this study are shown by grey squares (numbers next to squares correspond to dredge number in Tables 1 and 2 (Supplementary Dataset)).

depleted MORB to comparatively enriched MORB (e.g. K/Ti ratios as high as 0.3 are found). All samples isotopically resemble Indian Ocean MORB with radiogenic Sr and elevated $^{208}Pb/^{206}Pb$ relative to Pacific or Atlantic MORBs [10]. There is little or no evidence for involvement of Kerguelen/Heard or Amsterdam/St. Paul type mantle contributions to these basalts [10].

Graham et al. [11] showed that the general increase in ridge depth and decrease in mantle potential temperature (as traced by Fe_8 and Na_8) is also accompanied by a decrease in $^3He/^4He$; high $^3He/^4He$ ratios (up to 9.7 Ra) are associated with higher pressure, larger fraction melting compared to the low partial melt fractions found in AAD lavas that only have $^3He/^4He$ ratios of $\approx$6.5 Ra. These variations in $^3He/^4He$ could result from either a layered upper mantle—such that higher $^3He/^4He$ ratios occur at greater mantle depths—or from melting of discrete ^4He-rich pyroxenitic 'blebs' which are progressively diluted with 'normal' mantle He at high partial melt fractions [11].

3. Technique

The analytical technique used is that described in detail by Burnard et al. [27]. Large glassy chunks 5–8 mm diameter were cleaned in 10% nitric acid, water then ethanol, then loaded into online in vacuo crushing devices. Each sample was baked under vacuum at 120 °C for 6 h prior to sequential crushing at room temperature using an all-metal extraction system. The total volatiles released, which are predominantly CO_2 in MORBs [30], were analyzed using an MKS Baratron 222B 1-Torr capacitance manometer. After purification of active gases using two Zr–Al SAES NP10™ "getters", one at room temperature the other at 450 °C, Ar was separated from He and Ne using liquid N_2-cooled charcoal. Once desorbed off the charcoal, Ar was then analyzed using a 12-cm, 90° modified Nuclide noble gas mass spectrometer. He and Ne were trapped on charcoal at 14 K, then sequentially desorbed at 25 and 70 K, respectively, for analysis using a MAP215-50 noble gas mass spectrometer. Abundances were determined by peak-height comparison with an artificial noble gas standard made using reduced pressure air with added He, $^3He/^4He$=2.04 Ra, $^4He/^{40}Ar$=1.42. Calibrated volumes of the extraction system allowed He pressures to be reduced by either 77% or 93% in high $^4He/^{40}Ar$* samples. After crushing, samples were sieved to determine the crushing efficiency: normally about 25% of the sample passed through a 100-μm sieve.

Due to problems of vesicle preservation and heterogeneity which affect absolute noble gas compositions, it is desirable to normalize noble gas abundances to another volatile, notably CO_2: because CO_2 is the dominant volatile in MORBs, this is equivalent to noble gas abundances in the volatile phase. CO_2 was measured during the same crushing experiments as the noble gases; therefore, uncertainties associated with heterogeneous vesicle distributions are circumvented. Manometric CO_2 measurements can be problematic as powdering samples in the presence of CO_2 will result in adsorption of CO_2 on the powders, resulting in anomalously high noble gas/CO_2 ratios [27,28,31]. However, the effects of CO_2 absorption are minimal, provided the CO_2 release is sufficiently large and the samples are not completely powdered; crushing efficiency was deliberately kept low to prevent undue CO_2 adsorption on the glass powder [27,28]. The last crush step of each sample will have the most powder present in the crusher, as well as low CO_2 releases, increasing the potential for adsorption of a significant proportion of the CO_2 released. $^{40}Ar^*/CO_2$ and $^4He/CO_2$ in the final crush steps of each sample are anomalously high compared to the earlier crushing steps, consistent with CO_2 adsorption. However, excluding the last crush, the reproducibility of $^4He/CO_2$ and $^{40}Ar^*/CO_2$ of individual samples is ≤10%, which is more than adequate considering the factor 30 variation in $^4He/CO_2$ in the sample set as a whole.

4. Results

The abundances and isotope ratios of He, Ne and Ar, and the abundances of CO_2 released by multiple crushing of SEIR basaltic glasses are given in Table 2 (Supplementary Information).

4.1. Neon

As with all oceanic basalts, the Ne isotopic compositions of individual samples lie on a mixing line between atmospheric Ne and Ne with elevated $^{20}Ne/^{22}Ne$, $^{21}Ne/^{22}Ne$. High (more nucleogenic) $^{21}Ne/^{22}Ne$ would be expected in samples with radiogenic He (low $^3He/^4He$). Despite the fact that $^3He/^4He$ in some of these basalts are at the low end of the MORB range, it is not possible to distinguish Ne that is more nucleogenic than that found in MORBs, i.e. higher $^{21}Ne/^{22}Ne$ at a given $^{20}Ne/^{22}Ne$. Fig. 3 shows that the significant errors involved in measuring Ne isotopes—mostly due to large corrections at m/z=22 from CO_2^{2+}—mean that the small differences in slope between predicted nucleogenic Ne isotopic compositions for a mantle with $^3He/^4He$=5.5 Ra and the "normal" MORB trend (observed in MORBs with $^3He/^4He$=8 Ra) cannot be distinguished in this study.

4.2. Argon isotopes

As with Ne, there are large ranges in $^{40}Ar/^{36}Ar$ in multiple crushes of each sample, reflecting addition of a persistent atmospheric contaminant that is not completely removed by baking the sample in vacuo prior to analysis [32,33]; the highest ratio measured in each sample is most representative of the uncontaminated magmatic Ar. Individual segments display large ranges in $^{40}Ar/^{36}Ar$. It is likely that the $^{40}Ar/^{36}Ar$ ratio is determined by variable degrees of degassing combined with a relatively constant addition of atmospheric Ar, and therefore does not reflect changes in mantle $^{40}Ar/^{36}Ar$. The large $^{40}Ar/^{36}Ar$ range of individual ridge segments is therefore largely an artifact due to extent of degassing. The only firm constraint on the sub-SEIR mantle $^{40}Ar/^{36}Ar$ is that it must be higher than the highest ratio measured here (sample WW10-135-8: 20,000±2000). This is typical of MORBs [14].

4.3. Helium: external reproducibility

He isotopes and abundances were also measured at NOAA (Newport) in a previous study [11]. There is good agreement between $^3He/^4He$ measured at Caltech relative to ratios measured at NOAA, e.g. average $(^3He/^4He)_{NOAA}/(^3He/^4He)_{CIT}=0.98\pm0.02$. However, there is a marked difference between ^4He concentrations determined in the two laboratories, with He abundances measured at NOAA on average twice the CIT analyses of the same glass. This cannot be attributed to the poor efficiency of the CIT crushers which typically only reduce about 25% of the sample to <100 μm (Table 1, Supplementary Information) because experiments have shown that only 10–20% of the total He remains in the >100-μm fraction

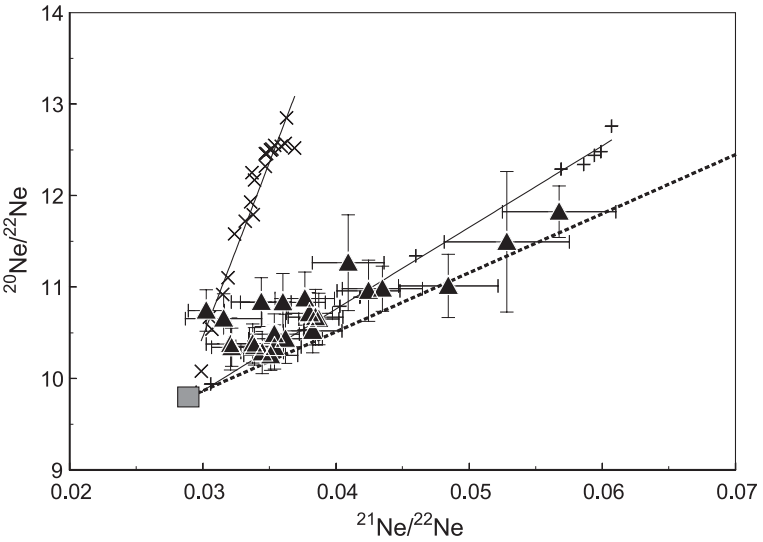

Fig. 3. Neon isotopes. Compositions of SEIR basalts (filled triangles) are plotted along with data from Iceland [54] ('×') and MORB (popping rock) [55] ('+') to illustrate the range in Ne isotope compositions observed in oceanic basalts; composition of air shown by large grey square. 1σ error bars are shown. Dashed line is calculated air–mantle mixing for a mantle source with $^{3}He/^{4}He$=5.5 Ra (the most radiogenic He found on the SEIR) and $^{3}He/^{22}Ne$=10 [56] (initial $^{4}He/^{3}He$=2000=350 Ra [57], initial $^{21}Ne/^{22}Ne$=0.033 [58], $^{21}Ne/^{4}He=2.5\times10^{-8}$ during nucleogenic production in the mantle [59]).

remaining after analysis (sieved residues of WW10-134 and WW10-76 were recrushed; Table 2, Supplementary Information). This is expected as the >100-μm fraction is mostly composed of grains ≪1 mm, whereas the noble gas budget is dominated by large (>500 μm) vesicles. It is more likely that the differences in He abundances are due to different sample processing in the two labs. Samples were not baked before analysis at NOAA and it is likely that some vesicles will have decrepitated during baking at Caltech. Differences between CIT and NOAA He concentrations can be accounted for by a single vesicle <0.7-mm radius at seafloor pressure which may have decrepitated during the CIT baking, but was included in the NOAA analysis. Given the high diffusivity of He in basaltic glasses [34], diffusive loss of He from the glasses during baking at CIT is possible. However, as only vesicle-trapped gases were analyzed in both studies, diffusive loss is less likely: a two-stage diffusion mechanism is required where the He in vesicles has to first dissolve into the already He saturated glasses before escaping through the glass. Furthermore, the large chips used will limit diffusive losses. The differences between the two datasets highlight the difficulties faced using noble gas *abundances* as a quantitative tool, particularly those involving inter-lab comparisons and it is possible that the most representative noble gas abundances (for isotopes that are readily corrected for atmospheric contamination) can only be measured in samples which have not been baked.

4.4. The highest $^{4}He/^{40}Ar^{*}$ in a MORB glass: sample WW10-76-1

The first analysis of WW10-76-1 had $^{4}He/^{40}Ar^{*}$ in excess of 500 (Table 2, Supplementary Information), considerably higher than previously measured in a MORB glass (previous maximum $^{4}He/^{40}Ar^{*}$=150 [35]). In order to confirm this result, two additional aliquots of the sample (each time starting with a new rind of uncrushed glass) were analyzed; while these still had very high $^{4}He/^{40}Ar^{*}$ (170 and 160; Table 2, Supplementary Information), these did not reproduce the first analysis. In case there was a vesicle size distribution issue ($^{4}He/^{40}Ar^{*}$ should be highest in the smallest vesicles; [26]), the "uncrushed" (>100-μm) residue from the second and third aliquots was combined and re-analyzed as aliquot 4. Again, although this fraction had slightly higher $^{4}He/^{40}Ar^{*}$

(180) compared to aliquots 2 and 3, the very high $^4He/^{40}Ar^*$ of the first aliquot was not reproduced. This sample is noticeably heterogeneous with an exterior rind composed of finely laminated glass layers and it remains possible that the first aliquot was a local heterogeneity; $^4He/^{40}Ar^*$ ratios are known to vary by more than a factor of 4 in a single pillow rind (from 9.6 to 42 [17]). Furthermore, the composition of the first aliquot is consistent with the general degassing trends observed in the sample set as a whole (for example, it lies on the same trend in plots of $^4He/^{40}Ar^*$ vs. $[^{40}Ar^*]$ and $^4He/^{40}Ar^*$ vs. $CO_2/^{40}Ar^*$), suggesting that this result was not due to analytical problems. However, until the analysis is duplicated, $^4He/^{40}Ar^*$ as high 500 in MORBs cannot be confirmed.

5. Discussion

5.1. Degassing

It is clear from Fig. 4 that the main control on noble gas relative abundances, and the absolute abundances of CO_2 and $^{40}Ar^*$, in these samples is magmatic degassing; the excellent correlation between $\ln(^4He/^{40}Ar^*)$ and $\ln(^{40}Ar^*)$ is entirely consistent with solubility controlled fractional (or Rayleigh) degassing with relative solubilities within the range determined experimentally (see Fig. 4 caption for more details). Batch degassing models (e.g. [24,25]) (using experimentally determined solubilities) have difficulties reproducing the extent of He/Ar fractionation that we observe in these samples.

While the range in $^4He/^{40}Ar^*$, $^{40}Ar^*/CO_2$, etc. result from fractionation during magmatic degassing, there must be an underlying mechanism that controls the extent of gas loss from each sample. Increasing gas loss can be achieved by either (a) reducing the CO_2 solubility of the melt or (b) by increasing the CO_2 concentration in the melt. Reducing pressure will reduce CO_2 solubility, therefore, CO_2 solubility will decrease during ascent and/or eruption of the basalts, whereas fractional crystallization will produce a net increase in CO_2 concentration in the melt (because CO_2 behaves as an incompatible element) [23,27]. These possible causes have specific outcomes that are discussed below.

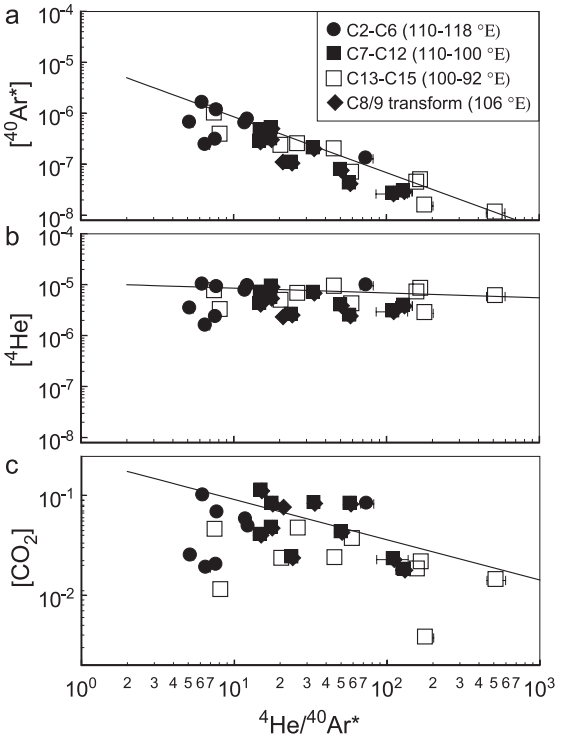

Fig. 4. Degassing of (a) Ar, (b) He and (c) CO_2 using $^4He/^{40}Ar^*$ as a degassing tracer. $[CO_2]$, $[^4He]$ and $[^{40}Ar^*]$ in cm^3 STP g^{-1}. Filled circles: C2–C6, filled squares: C7–C12, open squares: C13–C15, filled diamond: C8/9 transform. Note that the He and Ar axes are on the same scale to illustrate the effect of Ar insolubility on the degassing process. Solid lines are *modeled* degassing using published He–Ar–CO_2 solubilities [20] but starting compositions have been adjusted to fit the $^{40}Ar^*$ data (starting conditions: $[^{40}Ar^*]=5\times10^{-6}$ cm^3 STP g^{-1}, $^4He/^{40}Ar^*=2$, $^{40}Ar^*/CO_2=2.9\times10^{-5}$). From least squares fit $^4He/^{40}Ar^*=-0.79[^{40}Ar^*]-9.2$ ($R^2=0.83$), which (assuming Rayleigh degassing) corresponds to $S_{He}/S_{Ar}=8.5$ ($^{+2.9}_{-5}$), overlapping experimental values [20] and values estimated for degassing at the Amsterdam–St. Paul Plateau (cf. $S_{He}/S_{Ar}=5.8$ ($^{+1.7}_{-2.7}$) by Burnard et al. [27]).

5.1.1. Confining pressure at eruption

The confining pressure at eruption due to the overlying seawater—i.e. the eruption depth—is known to control the amount of volatiles trapped in submarine basaltic glasses [27,30,36], suggesting that magmatic gases are lost during eruption. In this scenario, the $^4He/^{40}Ar^*$ ratio should also be related to the eruption depth. However, along this 2000-km section of the SEIR, there is no clear relation between eruption pressure and $^4He/^{40}Ar^*$ ratio (Fig. 5), as would be expected if gas was lost during eruption. High $^4He/^{40}Ar^*$ ratios are found in shallow erupted—

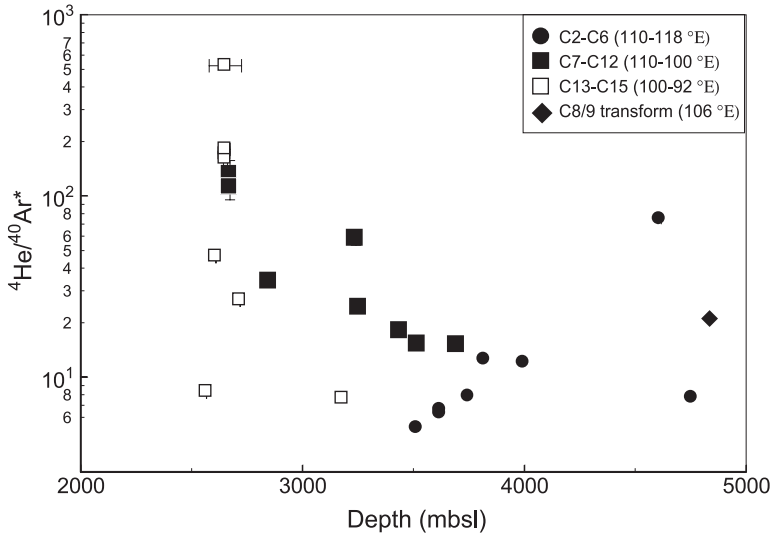

Fig. 5. $^{4}He/^{40}Ar^{*}$ vs. ridge depth. Symbols as in Fig. 4. Degassing (traced by the $^{4}He/^{40}Ar^{*}$ ratio) increases with decreasing eruption depth (≡eruption pressure) in segments C7 through C12, as may be predicted if significant degassing occurred during eruption. However, this behavior abruptly changes east of segment 7 (east of 100 °E), where the $^{4}He/^{40}Ar^{*}$ ratio appears to decrease in shallow erupted samples, suggesting that (a) degassing during eruption was not significant and (b) some other mechanism—possibly one that would increase with increasing depth—fractionates He from Ar. The western segments (C13–C15) have a considerable range in $^{4}He/^{40}Ar^{*}$ with little variation in eruption depth (of the samples studied). These changes in degassing style coincide with changes in ridge morphology: west of 100 °E (open squares) is characterized by an axial high, whereas an axial trough is present east of 110 °E (filled circles). In between (110–100 °E, filled squares), there is an intermediate ridge morphology without either pronounced ridge or trough [37].

samples for some specific ridge segments, for example, segment C8 (excluding the C8/C9 transform) although this is not true for the entire length of ridge studied. The eruption pressure is not the dominant control on volatile loss in these samples.

5.1.2. Combined fractional crystallization–degassing

In some oceanic basalts, the degree of degassing appears to be related to the extent of fractional crystallization. CO_2 is expected to behave incompatibly; therefore, the CO_2 concentration in the melt will increase during fractional crystallization, thereby increasing the fraction of gas lost from the melt [23,27]. This process is thought to have produced correlations between $^{4}He/^{40}Ar^{*}$, which traces the extent of degassing, and indices of crystallization, such as Mg#, in basalts from the Amsterdam–St. Paul Plateau [27] and in MORBs globally [23]. However, there is no correlation between $^{4}He/^{40}Ar^{*}$ and Mg# (not shown) in the SEIR samples analyzed here, despite similar degrees of fractional crystallization and gas concentrations to the Burnard et al. [27] study of the ASP plateau (e.g. $[CO_2]_{ASP}$=0.003–0.074, $[CO_2]_{SEIR}$=0.004–0.11 cm^3 STP g^{-1}, lowest Mg# in ASP=50, lowest Mg# SEIR=50). "Crystallization forced" degassing does not appear to be an important process on the SEIR east of the ASP plateau, although the reasons for this are not clear.

In summary, the absolute and relative volatile abundances of these samples have been affected by volatile loss prior to and during emplacement on the seafloor. The volatile loss can be adequately modeled as solubility controlled fractional degassing. Overall, however, there seem to be several underlying causes to the gas loss along the ridge which may be related to variations in ridge morphology (Fig. 5, [37]). Gas loss along some segments is apparently controlled by confining pressure on eruption but along other segments, shallow eruptions do not result in extensive degassing.

5.2. Estimating the parental magma composition

It is clear that noble gas relative and absolute abundances, and $^{40}Ar^{*}/CO_2$ ratios (Fig. 4), are predominantly controlled by magmatic degassing. The

[^{40}Ar*], ^{4}He/^{40}Ar* and ^{40}Ar*/CO_2 compositions can be adequately modeled as fractional degassing using experimentally determined solubilities (Fig. 4, Section 5.1). It should, therefore, be possible to invert the degassing process (irrespective of the actual mechanism involved) in order to estimate "pre-degassing" magmatic compositions. From Fig. 6, it is evident that, at a given ^{40}Ar*/CO_2, the ^{4}He/^{40}Ar* ratios of samples from the more shallow (western) end of the SEIR are higher than those of the eastern end. The fact that there are systematic differences above experimental error in a plot of two degassing tracers (e.g. Fig. 6) requires that either there were variations in the ^{40}Ar–^{4}He–CO_2 compositions prior to degassing, or there were large differences in the degassing trajectories of individual samples (i.e. the slope in Fig. 6).

Here, we have attempted to estimate the "pre-degassing" ^{4}He/^{40}Ar* ratio by assuming the slope in a plot of ^{4}He/^{40}Ar* vs. ^{40}Ar*/CO_2 is that predicted by fractional degassing using previously published volatile solubilities [20]. This is illustrated in Fig. 6. However, very similar results are obtained if the slope defined by a best fit through this dataset is used instead of the experimentally predicted fractionation slope. A similar degassing correction scheme is illustrated in [6,26].

The major drawback to using this technique to correct for magmatic degassing is the uncertainty in choosing an initial volatile composition that can be used as reference (in the way that fractional crystallization is corrected back to 8 wt.% MgO, for example). Ideally, it should be possible to use the initial ^{4}He/^{21}Ne* ratio, as advocated by Burnard [6,26]. Unfortunately, the errors involved in our ^{21}Ne* measurements were too large and this method cannot be applied to these data. Instead, we have corrected all degassing trajectories to the same ^{40}Ar*/CO_2 ratio, estimated from the extrapolations in Fig. 4 (see Fig. 4 caption), in order to estimate the "pre-degassing" ^{4}He/^{40}Ar* ratio. Although the initial

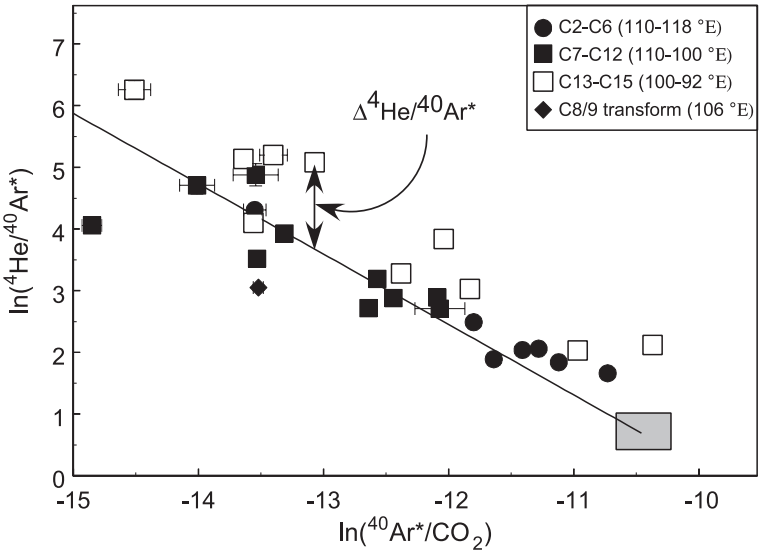

Fig. 6. Pre-degassing fractionation of He–Ar–CO_2. Symbols as in Fig. 4. Degassing of a single mantle-like composition (given by the solid rectangle: ^{40}Ar*/CO_2=2.9×10^{-5}, ^{4}He/^{40}Ar*=2) will reduce ^{40}Ar*/CO_2 and increase ^{4}He/^{40}Ar* along the trajectory given by the solid line, which is the calculated fractional degassing path starting from mantle compositions (S_{He}/S_{Ar}=11.6, S_{Ar}/S_{CO_2}=0.37 calculated from [20,60]). Although there is a reasonable correlation between ^{4}He/^{40}Ar* and ^{40}Ar*/CO_2, it is clear there are systematic differences between ridge segments, for example the western segments (C13–C15, open squares) systematically plot above the theoretical trajectory, while the eastern segments plot on or below the line. This suggests that there was fractionation of the He–Ar–CO_2 system prior to magmatic degassing. The amount of "pre-degassing" He–Ar fractionation is quantified by assuming that the initial ^{40}Ar*/CO_2 was constant and that the vertical difference between the theoretical degassing line (solid line in the figure) is due to variations in the initial ^{4}He/^{40}Ar* ratio. The "degassing corrected" ^{4}He/^{40}Ar* ratio is referred to as "Δ^{4}He/^{40}Ar$^{*}_{init}$" because, while the initial ^{40}Ar*/CO_2 for the theoretical degassing trajectory is a reasonable guess for the mantle (e.g. corresponds to C/^{3}He in the mantle of 1.5×10^{9} if the mantle ^{4}He/^{40}Ar* is 2), the true mantle ^{40}Ar*/CO_2 value is unknown.

$^{40}Ar^*/CO_2$ ratio used here (2.9×10^{-5}) is a reasonable guess for typical depleted mantle [23], it is not known if this value is appropriate for the SEIR; consequently, the "initial" $^4He/^{40}Ar^*$ ratio estimated in this way is only an estimate of *relative* fractionation and therefore is denoted $\Delta^4He/^{40}Ar^*_{init}$.

5.2.1. Problems correcting for degassing

It is clear that variations in the pre-degassing ^4He–$^{40}Ar^*$–CO_2 compositions of the SEIR magmas do exist. In order to quantify the extent of these variations we have assumed there is no variation in $^{40}Ar^*/CO_2$ and all the variation is in $^4He/^{40}Ar^*$. This is unlikely to be strictly true as mantle heterogeneities in $^{40}Ar^*/CO_2$ do exist [23], and processes operating in the mantle which fractionate He from Ar could also fractionate Ar from CO_2. However, it seems likely that the majority of the variation in initial He–Ar–CO_2 compositions will be in the He/Ar ratio rather than the Ar/CO_2 ratio: variations in initial $^{40}Ar^*/CO_2$ in MORBs generally appear to be small (<factor 2 [23]) relative to the large (factor ≈ 100) variations observed in this suite of basalts which are due to degassing. In order to account for the "pre-degassing" variation in He–Ar–CO_2 in these magmas solely through $^{40}Ar^*/CO_2$ variability (i.e. assuming the pre-degassing $^4He/^{40}Ar^*$ was constant) requires that the ratio (He or Ar)/CO_2 varies by a factor of ≈ 20 over this section of the ridge. Large variations of this ratio in the mantle are most plausibly related to recycling of carbon-rich sediments, yet there is no evidence of large variations in the amount of recycled material in the Sr or Pb isotope compositions of these basalts [10]. Therefore, it seems likely that most of the variation in the pre-degassing He–Ar–CO_2 compositions is in the He/Ar ratio rather than the (He or Ar)/CO_2 ratio. Nevertheless, it is important to bear in mind that "$\Delta^4He/^{40}Ar^*_{init}$" carries with it the collective variation in the pre-degassing He–Ar–CO_2 compositions, rather than being solely a reflection of the $^4He/^{40}Ar$ ratio prior to degassing.

The initial $^4He/^{40}Ar^*$ ratio calculated this way is relatively insensitive to initial $^{40}Ar^*/CO_2$: a variation of ≈2 in the initial $^{40}Ar^*/CO_2$ will have a negligible effect on the computed $\Delta^4He/^{40}Ar^*_{init}$; for example, the shaded box in Fig. 6 encompasses the range in $^{40}Ar^*/CO_2$ reported for 'normal' MORBs ($2–4\times10^{-5}$) [23].

The corrections for degassing also assume that the relative He–Ar–CO_2 solubilities do not change significantly during degassing.

5.3. ^4He–$^{40}Ar^*$ variations in primary melts

The results of performing these degassing corrections is that there appear to be real variations in $\Delta^4He/^{40}Ar^*_{init}$; if the initial $^{40}Ar^*/CO_2$ used here is correct and constant, then the actual $^4He/^{40}Ar^*_{init}$ ratios of primary melts along the SEIR vary between 2 and 12, with the highest $\Delta^4He/^{40}Ar^*_{init}$ values limited to the western end of the section studied.

Surprisingly, there is a relationship between $\Delta^4He/^{40}Ar^*_{init}$ and the $^3He/^4He$ ratio (Fig. 7); with the exception of sample WW10-126-1, high $^3He/^4He$ ratios are found in primary magmas that have high $^4He/^{40}Ar$; there is considerable variation in $\Delta(^4He/^{40}Ar^*)_{init}$ within segments C7–C12 at relatively constant $^3He/^4He$, despite the overall positive correlation (Fig. 7). $\Delta^4He/^{40}Ar^*_{init}$ also decreases with the general increase in average ridge depth eastward along the SEIR (not shown). The relationship between $\Delta^4He/^{40}Ar^*_{init}$ and $^3He/^4He$ existed prior to magmatic degassing: if degassing produced these co-variations (for example, if high $^3He/^4He$ magmas coincidentally degassed more extensively, thereby also fractionating He from Ar more extensively), then a correlation between the *uncorrected* $^4He/^{40}Ar^*$ ratio and $^3He/^4He$ would be expected, whereas there is no discernable relationship between $^3He/^4He$ and uncorrected $^4He/^{40}Ar^*$ (not shown). Possible causes of the variation in $\Delta^4He/^{40}Ar^*_{init}$ and the correlation between $\Delta^4He/^{40}Ar^*_{init}$ and $^3He/^4He$ are investigated below.

5.3.1. Fractionating, post-eruptive He loss

It is possible that some of the range in $\Delta^4He/^{40}Ar^*_{init}$ and $^3He/^4He$ result from diffusive loss of He from the basalts after eruption; post-eruptive diffusive fractionation of He from Ar has been previously postulated [38]. If post-eruptive He loss was accompanied by He isotope fractionation, then this would result in a positive correlation between $^3He/^4He$ and the calculated "$\Delta^4He/^{40}Ar^*_{init}$". While He diffusion at seafloor temperatures is probably sufficiently slow to prevent significant He loss, there is potential for diffusion of He out of the erupting lava during chilling on the seafloor, or from subsequent reheating during later emplacement

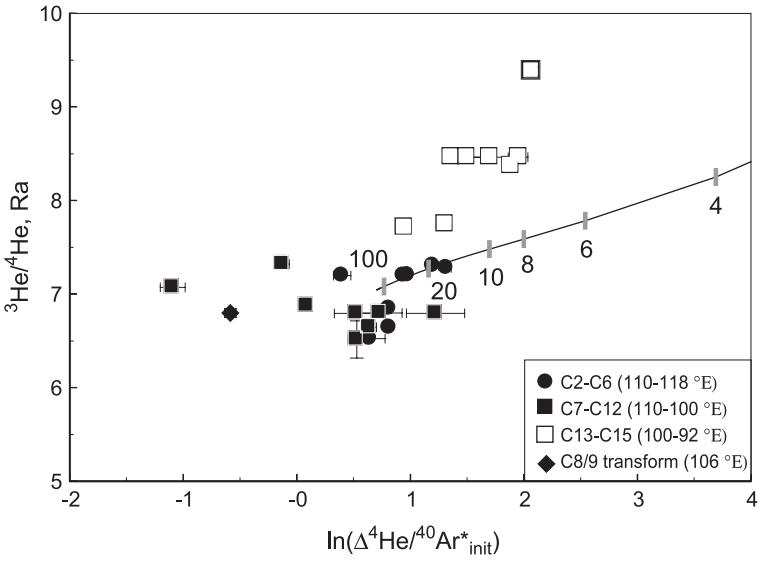

Fig. 7. $\Delta^4He/^{40}Ar^*$ vs. $^3He/^4He$; note that $\Delta^4He/^{40}Ar^*$ is in natural log units. Symbols as in Fig. 4. The $^3He/^4He$ ratios used are those reported for the same samples by [11] as these have smaller uncertainties than the data obtained here. The uncertainty in $\Delta^4He/^{40}Ar^*$ (1σ error bars) only accounts for measurement errors and does not include uncertainties in relative solubilities when making the degassing correction. The line shows the predicted fractionation of $^3He/^4He$ and $^4He/^{40}Ar^*$ due to diffusion following Burnard [6] (numbers correspond to $t/l^2\times10^{-6}$ years cm^{-2}). The most fractionated samples require $t/l^2 \approx 6\times10^{-5}$ years cm^{-2}; if a fracture spacing of 100 cm is present in the mantle, $t/l^2=6\times10^{-5}$ years cm^{-2} corresponds to ≈0.5 year of melt residence in the fracture.

of lavas. However, it is difficult to envisage a post-eruptive mechanism which would produce a relationship between $^3He/^4He$ and Fe_8 as observed in these lavas [11]; therefore, post-eruptive diffusive fractionation of $^3He/^4He$ ratios seems unlikely.

5.3.2. Artifacts introduced in the degassing correction

Noble gas relative solubilities in basaltic liquids are known to be a function of the water (and, to a lesser extent, CO_2) content of the melts [22,39]. It is possible that variations in water content modified the slope of the degassing trajectory, and, as a result, the variations in $\Delta^4He/^{40}Ar^*_{init}$ are merely artifacts of erroneous degassing corrections. For example, all samples may have started with the same $^4He/^{40}Ar^*$ and $^{40}Ar^*/CO_2$ compositions, but do not lie on a single line in Fig. 6 due to differences in degassing trajectory from one sample to the next, and these differences in degassing trajectory are related to the source chemistry and $^3He/^4He$. Realistically, the variations in degassing trajectories that are required are impossibly large, requiring several hundred percent change in the relative He/Ar and Ar/CO_2 solubilities. Unless there is an as yet undiscovered major change in CO_2 solubility mechanism, then increases in CO_2 solubility are accompanied by increases in both He and Ar solubility, resulting in approximately constant relative He/CO_2 and Ar/CO_2 solubilities.

It seems inescapable that there are variations in the volatile compositions prior to magmatic degassing.

5.3.3. Two-stage degassing models

Cartigny et al. [40] and Shaw et al. [39] proposed that degassing in oceanic basalts may occur in two stages. The first stage is the formation of bubbles in a batch process within the mantle, while the second stage is open system degassing which results from decompression in the crust. The effects of the first stage of degassing will affect the $\Delta^4He/^{40}Ar^*_{init}$ compositions computed above because the correction procedure used only accounts for fractionation occurring during the second, fractional degassing stage. Thus, it is possible that the variation in $\Delta^4He/^{40}Ar^*_{init}$ observed in these lavas results from variable degrees of bubble formation prior to fractional degassing. The magnitude of the shift in $\Delta^4He/^{40}Ar^*_{init}$ will depend on the fraction volatiles lost during the first phase. The maximum possible shift in $\Delta^4He/^{40}Ar^*_{init}$ is ≈10 (the

ratio of the He and Ar solubilities). However, while two-stage degassing may have occurred in the SEIR magmas, this is unlikely to be the cause of the correlated $^3He/^4He$ and $\Delta^4He/^{40}Ar^*_{init}$ for two reasons: (a) equilibrium degassing is unlikely to fractionate He isotopes and therefore would not result in the correlation in Fig. 7 and (b) the range in $\Delta^4He/^{40}Ar^*_{init}$ observed is greater than that possible during the first stage of degassing.

5.3.4. ^{4}He and ^{40}Ar production in chemical heterogeneities within the mantle

Graham et al. [11] suggested that melting of U-rich pyroxenitic heterogeneities in the sub-SEIR mantle could result in the low $^3He/^4He$ observed in the AAD; these pyroxenitic "blebs" melt at a lower temperature than ambient mantle, consequently they will constitute a larger proportion of the melt at lower partial melt fraction, hence low $^3He/^4He$ results from melting colder mantle. Furthermore, the majority of the variation in Fig. 7 results from samples from the western end of the ridge segment studied, and it is possible a localized mantle heterogeneity, with relatively high $^3He/^4He$ ratios, exists in this region. Could melting of these chemical and isotopic heterogeneities also explain variations in $\Delta^4He/^{40}Ar^*_{init}$ observed along the SEIR?

In order for chemical heterogeneity to account for the correlation in Fig. 7, then:

(a) the low $^3He/^4He$ component must have low $^4He/^{40}Ar^*$;
(b) assuming that low $^3He/^4He$ results from heterogeneities within the mantle, then these heterogeneities must also have $^4He/^{40}Ar^*$ lower than ambient mantle; and
(c) $(^4He/^{40}Ar^*)_{ambient}/(^4He/^{40}Ar^*)_{heterogeneity} \geq 10$.

If the high $^3He/^4He$ component represents ambient mantle with an actual $^4He/^{40}Ar^*$ of 2–4 (corresponding to production from a mantle with $K/U=1.2\times10^4$ [41]), then, from (c), the low $^3He/^4He$ heterogeneities must have $^4He/^{40}Ar^*$ of 0.2–0.4. In order to generate such low $^4He/^{40}Ar^*$, the cpx blebs require $U/K \leq 1.5\times10^{-5}$ ($K/U \geq 6.5\times10^4$); this is assuming that the radiogenic He and Ar accumulated for 4 Ga. A more reasonable "age" of a recycled cpx bleb may be $\approx$1.5 Ga [42]; in this case, a U/K ratio around 7×10^{-6} ($K/U=1.4\times10^5$) is necessary. The above calculations assume a Th/U of 4.2.

Therefore, if the variations in $\Delta^4He/^{40}Ar^*_{init}$ result from a mantle heterogeneity, the heterogeneity should have a K/U ratio $\approx$10 times higher than that of the bulk upper mantle value (1.2×10^4). From Pb isotope evidence, the U/Pb ratio does not change drastically along this section of ridge [10]; therefore, it seems more likely that K addition (rather than U depletion) could increase the K/U ratio. Assuming that ^{36}Ar distribution is uniform, this would result in more radiogenic (higher) $^{40}Ar/^{36}Ar$ ratios in the cpx blebs; unfortunately, problems associated with atmospheric contamination make it impossible to test this hypothesis using Ar isotopes.

Nevertheless, there is no relationship between $\Delta^4He/^{40}Ar^*_{init}$ and K/Ti (not shown), which would be expected if a K-rich geochemical heterogeneity resulted in the high $^4He/^{40}Ar^*$ ratios. Furthermore, given the constancy of K/U ratios in MORBs generally (for example, "depleted" MORBs and "enriched" MORBs have indistinguishable K/U, despite a factor of 10 difference in K concentration [43]) and the broadly similar partitioning behavior of U and K in cpx of mantle composition [44], an enrichment in K/U of at least a factor of 5 seems unlikely.

5.3.5. Kinetic fractionation of He and Ar during melt–wallrock infiltration

Models by Torgersen and O'Donnell [45] and experiments by Honda et al. [46] have shown that He diffusion out of a newly formed fracture will be considerably greater than that of Ar; He/Ar ratios in the fracture can be up to 10^4 times that of the source rock at geologically reasonable conditions. Melt localized in channels within the mantle [47–52] introduces the potential for diffusive fractionation of He from Ar within the mantle. This process was examined by Burnard [6] who showed that fractionation of He isotopes should occur, in addition to He–Ar fractionation during diffusion from the solid mantle into the melt, due to the predicted difference in diffusivity between ^{3}He and ^{4}He [53]. In theory, large (factor of 10) variations in $^4He/^{40}Ar^*$ should be accompanied by small, but detectable variations in $^3He/^4He$ of the order 10% (assuming that the relative diffusivities of the noble gas isotopes are determined by the square root of the mass difference). Given that

it is difficult to account for the range in $\Delta^4He/^{40}Ar^*_{init}$ in the SEIR basaltic glasses using variations in mantle K/U, diffusive fractionation of He and Ar should be considered.

The low concentrations of noble gases in equilibrium mantle melts, combined with their high diffusivities in solids, increases the potential for observing diffusive fractionation during mantle melting. It seems likely that wallrock–melt diffusive fractionation effects are only apparent for the noble gases because all other mantle species are either slow diffusing or are present in high concentrations in the mantle. The degree of fractionation resulting from diffusion of noble gases out of solid mantle into melt channels (or, at least, fast diffusion pathways for the noble gases) depends primarily on t/l^2 where t is the time the fast diffusion pathway has been established and l is the separation between fast diffusion pathways (melt channels) [6]. In order to significantly fractionate He isotopes during diffusion of He from the solid into the melt, only a small fraction of He can be extracted from the mantle by volume diffusion: extraction of more than 1% of the He contained between two melt channels will result in negligible isotopic fractionation.

The models described in Burnard [6] predict that there should be a positive correlation between $\Delta^4He/^{40}Ar^*_{init}$ and $^3He/^4He$. Although there is a positive correlation between $\Delta^4He/^{40}Ar^*_{init}$ and $^3He/^4He$ in Fig. 7, the slope predicted by the diffusive fractionation model is significantly shallower than that observed in the SEIR data: the model predicts *less* He isotope fractionation for a given He–Ar fractionation compared to the variations observed. It is difficult to envisage a scenario where diffusive fractionation could result in greater He isotope fractionation (for a given He–Ar fractionation) than that predicted by the model: by assuming "square root of mass difference" behavior, the purpose of the diffusive fractionation model was to investigate the *maximum* possible He isotopic fractionation for a given He–Ar fractionation.

Furthermore, during diffusive fractionation of noble gases, He and Ar in the primary magmas will be a mixture of diffusively inherited noble gases and unfractionated noble gases generated by the equilibrium partial melting that produced the silicates. The greatest $\Delta^4He/^{40}Ar^*_{init}$ values are expected in the lowest degree partial melts, where the fraction of noble gases derived from equilibrium partial melting of the mantle will be least significant. This predicts a positive correlation between $^4He/^{40}Ar^*$ and Na_8; however, Fig. 8 shows that, although there is no correlation between $^4He/^{40}Ar^*$ and Na_8, the greatest ^4He–$^{40}Ar^*$ fractionation occurs in high degree partial

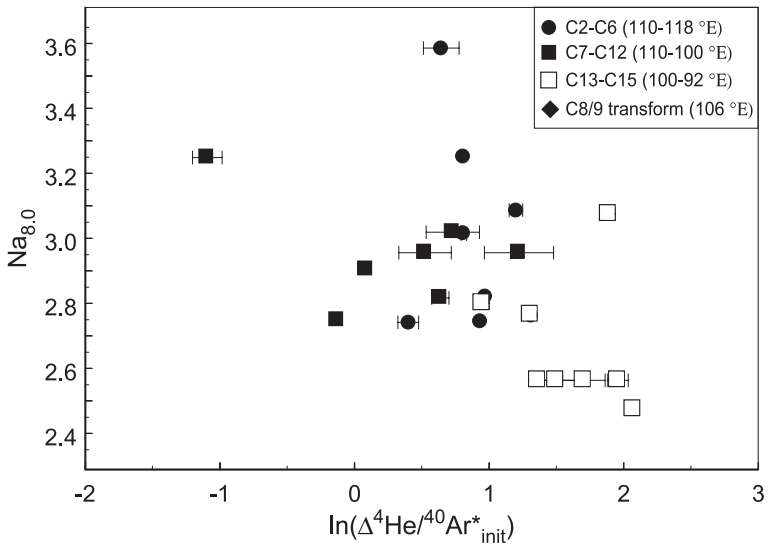

Fig. 8. $\Delta^4He/^{40}Ar^*_{init}$ vs. Na_8. Symbols as in Fig. 4. Na_8 data from [61]. The most He–Ar fractionation during melting (i.e. highest $\Delta^4He/^{40}Ar^*_{init}$) occurs in basalts with the lowest Na_8 values, i.e. those derived by the greatest extent of melting.

melts (assuming that the Na_8 variations are not related to chemical or mineralogical heterogeneities in the mantle), contrary to the prediction. It is possible that diffusive fractionation of $^4He/^{40}Ar^*$ in the mantle depends on other parameters (e.g. t/l^2), which may counter balance the diluting effect of large melt fractions, e.g. low degree partial melts could take longer to extract from the mantle (due to a greater tortuosity, for example), increasing t/l^2 and thereby resulting in less diffusive fractionation (more equilibration) of $^4He/^{40}Ar^*$ in low degree partial melts.

In conclusion, some process (or processes) acting in the mantle produced melts with a large range in $^4He/^{40}Ar$ which was correlated with the $^3He/^4He$ ratio (with the possible exception of segments C7–C12). However, the mechanism(s) producing these variations remains enigmatic. On the one hand, equilibrium melting of a geochemical heterogeneity is unlikely to create the very low $\Delta^4He/^{40}Ar^*_{init}$ values, while fractionation by diffusion from the solid mantle into the melt cannot create the full range in He isotope composition observed. It is plausible that a combination of the two processes resulted in the correlation between $^3He/^4He$ and $\Delta^4He/^{40}Ar^*_{init}$. For example, a low $^3He/^4He$ eclogitic heterogeneity in the mantle will likely have different melting parameters than 'normal' depleted MORBs, which may increase diffusive fractionation of He from Ar, creating the correlation observed in Fig. 7.

6. Summary

The large variations in $^{40}Ar^*$ concentrations, $^{40}Ar^*/CO_2$ and $^4He/^{40}Ar^*$ in the SEIR basaltic glasses can be attributed to variable extents of degassing. The extent of degassing is not related to either the eruption depth or the extent of fractional crystallization in any simple way, in contrast to the Amsterdam–St. Paul's section of the SEIR [27].

Attempts to correct for the degassing processes using combined He–Ar–CO_2 data suggest that some variation in $^4He/^{40}Ar^*$ existed in the primary basalts prior to any magmatic degassing, and the $^4He/^{40}Ar^*$ of the primary melts ($\Delta^4He/^{40}Ar^*_{init}$) correlates with $^3He/^4He$.

Equilibrium distribution of He and Ar during melting are unlikely to produce the fractionation as both are similarly incompatible [1] and the relatively large degrees of partial melting at mid-ocean ridges are unlikely to fractionate incompatible elements. Therefore, these compositional variations are more likely to be related to either kinetic He–Ar fractionation during mantle melting or to long-lived chemical heterogeneities within the mantle, or a combination of both processes.

Although diffusion models show that, if He fractionates from Ar by diffusion, then some fractionation of He isotopes should also be expected as ^3He diffuses faster than ^4He [53]. However, modeling suggests that diffusive fractionation will not be able to produce the observed range in $^3He/^4He$ (for a given $^4He/^{40}Ar^*$) and it seems more likely that the range in $^3He/^4He$ results from sampling a heterogeneous mantle, for example, sampling eclogitic material with more radiogenic He than the ambient mantle. However, mantle heterogeneities are unlikely to produce the range in $^4He/^{40}Ar^*$ (corrected for magmatic degassing) observed, because K and U do not appear to fractionate significantly during mantle processes [43]. In this case, it does appear more likely that kinetic fractionation of He from Ar did occur during mantle melting, and that this fractionation is greatest when melting the non-eclogitic portions of the mantle, resulting in high $^3He/^4He$ magmas with high He/Ar ratios.

Although the processes producing correlations between noble gas relative abundances (e.g. $\Delta^4He/^{40}Ar^*_{init}$) and He isotopes in the SEIR primary melts remain uncertain, the ability to correct for noble gas fractionation during magmatic degassing opens the way for future work investigating relative noble gas abundances of primary melting. In particular, possible kinetic fractionation of He isotopes during mantle melting has implications beyond the scope of the present contribution, such as isotopic fractionation during mantle metasomatic processes and, with appropriate parameterization, the possibility of using kinetic fractionation of noble gases for constraining models of mantle melting and transport.

Acknowledgements

This work was supported by the Marine Geology and Geophysics Division of the National Science Foundation (OCE99-12359 and OCE99-11418). Dave

Christie (OSU) helped with sample selection and shared major and trace element data. The authors are extremely grateful for the thorough and insightful reviews by Dave Hilton, Manuel Moreira, Phillipe Sarda and an anonymous reviewer.

Appendix A. Supplementary data

Supplementary data associated with this article can be found, in the online version, at doi: 10.1016/j.epsl.2004.08.021.

References

[1] R.A. Brooker, Z. Du, J.D. Blundy, S.P. Kelley, N.L. Allan, B.J. Wood, E.M. Chamorro, J.A. Wartho, J.A. Purton, The 'zero charge' partitioning behaviour of noble gases during mantle melting, Nature 423 (2003) 738–741.

[2] E.M. Chamorro, J.A. Wartho, R.A. Brooker, S.P. Kelley, B.J. Wood, Noble Gases Partition Coefficients between clinopyroxene–silicate melt at high pressure, Eos Transactions, American Geophysical Union, 80, American Geophysical Union, Washington, 1999, pp. 1123.

[3] E.M. Chamorro, R.A. Brooker, J.A. Wartho, B.J. Wood, S.P. Kelley, J.D. Blundy, Ar and K partitioning between clinopyroxene and silicate melt to 8 GPa, Geochim. Cosmochim. Acta 66 (2002) 507–519.

[4] J.-i. Matsuda, B. Marty, The $^{40}Ar/^{36}Ar$ ratio of the undepleted mantle; a reevaluation, Geophys. Res. Lett. 22 (1995) 1937–1940.

[5] M. Honda, D.B. Patterson, Systematic elemental fractionation of mantle-derived helium, neon, and argon in mid-oceanic ridge glasses, Geochim. Cosmochim. Acta 63 (1999) 2863–2874.

[6] P. Burnard, Diffusive fractionation of noble gases and helium isotopes during mantle melting, Earth Planet. Sci. Lett. 220 (2004) 287–295.

[7] J.-C. Sempere, J.R. Cochran, The Southeast Indian Ridge between 88 degrees E and 118 degrees E; variations in crustal accretion at constant spreading rate, J. Geophys. Res. 102 (1997) 15489–15505.

[8] E.M. Klein, C.H. Langmuir, A. Zindler, H. Staudigel, B. Hamelin, Isotope evidence of a mantle convection boundary at the Australian–Antarctic Discordance, Nature 333 (1988) 623–629.

[9] E.M. Klein, C.H. Langmuir, H. Staudigel, Geochemistry of basalts from the Southeast Indian Ridge, 115 degrees E–138 degrees E, J. Geophys. Res. B 96 (1991) 2089–2107.

[10] J.J. Mahoney, D.W. Graham, D.M. Christie, K.T.M. Johnson, L.S. Hall, D.L. Vonderhaar, Between a hotspot and a cold spot; isotopic variation in the Southeast Indian Ridge asthenosphere, 86 degrees E–118 degrees E, J. Petrol. 43 (2002) 1155–1176.

[11] D.W. Graham, J.E. Lupton, F.J. Spera, D.M. Christie, Upper-mantle dynamics revealed by helium isotope variations along the Southeast Indian ridge, Nature 409 (2001) 701–703.

[12] E.M. Klein, C.H. Langmuir, Global correlations of ocean ridge basalt chemistry with axial depth and crustal thickness, J. Geophys. Res. 92 (1987) 8089–8115.

[13] C.J. Allègre, T. Staudacher, P. Sarda, Rare gas systematics: formation of the atmosphere, evolution and structure of the Earth's mantle, Earth Planet. Sci. Lett. 81 (1986) 127–150.

[14] D.W. Graham, Noble gas isotope geochemistry of mid-ocean ridge and ocean island basalts; characterization of mantle source reservoirs, Rev. Mineral. Geochem. 47 (2002) 247–317.

[15] P.H. Sarda, D. Graham, Mid-ocean ridge popping rocks: implications for degassing at ridge crests, Earth Planet. Sci. Lett. 97 (1990) 268–289.

[16] H. Kumagai, I. Kaneoka, Variations of noble gas abundances and isotope ratios in a single MORB pillow, Geophys. Res. Lett. 25 (1998) 3891–3894.

[17] H. Kumagai, I. Kaneoka, Relationship between submarine MORB glass textures and atmospheric component of MORBs, Chem. Geol. 200 (2003) 1–24.

[18] P. Burnard, The bubble-by-bubble volatile evolution of two mid-ocean ridge basalts, Earth Planet. Sci. Lett. 174 (1999) 199–211.

[19] T. Shibata, E. Takahashi, J.-i. Matsuda, Solubility of neon, argon, krypton, and xenon in binary and ternary silicate systems; a new view on noble gas solubility, Geochim. Cosmochim. Acta 62 (1998) 1241–1253.

[20] M.R. Carroll, E.M. Stolper, Noble gas solubilities in silicate melts and glasses: new experimental results for argon and the relationship between solubility and ionic porosity, Geochim. Cosmochim. Acta 57 (1993) 5039–5052.

[21] P.M. Nuccio, A. Paonita, Investigation of the noble gas solubility in H_2O–CO_2 bearing silicate liquids at moderate pressure: II. The extended ionic porosity (EIP) model, Earth Planet. Sci. Lett. 183 (2000) 499–512.

[22] A. Paonita, G. Gigli, D. Gozzi, P.M. Nuccio, R. Trigila, Investigation of the He solubility in H (sub 2) O–CO (sub 2) bearing silicate liquids at moderate pressure; a new experimental method, Earth Planet. Sci. Lett. 181 (2000) 595–604.

[23] B. Marty, L. Zimmerman, Volatiles (He, C, N, Ar) in mid-ocean ridge basalts: assessment of shallow level fractionation and characterization of source composition, Geochim. Cosmochim. Acta 63 (1999) 3619–3633.

[24] M. Moreira, P. Sarda, Noble gas constraints on degassing processes, Earth Planet. Sci. Lett. 176 (2000) 375–386.

[25] P. Sarda, M. Moreira, Vesiculation and vesicle loss in mid-ocean ridge basalt glasses: He, Ne, Ar elemental fractionation and pressure influence, Geochim. Cosmochim. Acta 66 (2002) 1449–1458.

[26] P. Burnard, Correction for volatile fractionation in ascending magmas; noble gas abundances in primary mantle melts, Geochim. Cosmochim. Acta 65 (2001) 2605–2614.

[27] P.G. Burnard, D.W. Graham, K.A. Farley, Mechanisms of magmatic gas loss along the Southeast Indian Ridge and the Amsterdam–St. Paul Plateau, Earth Planet. Sci. Lett. 203 (2002) 131–148.

[28] P.G. Burnard, D.W. Harrison, G. Turner, R. Nesbitt, Degassing and contamination of noble gases in Mid-Atlantic Ridge basalts, Geochem. Geophys. Geosysts. 4 (2003) DOI:10.1029/2002GC000326.
[29] M. Manga, H.A. Stone, Interactions between bubbles in magmas and lavas; effects of bubble deformation, J. Volcanol. Geotherm. Res. 63 (1994) 267–279.
[30] J.G. Moore, Vesicularity and CO_2 in mid-ocean ridge basalt, Nature 282 (1979) 250–253.
[31] C. Barker, B.E. Torkelson, Gas adsorption of crushed quartz and basalt, Geochim. Cosmochim. Acta 55 (1975) 212–218.
[32] C.J. Ballentine, D.N. Barfod, The origin of air-like noble gases in MORB and OIB, Earth Planet. Sci. Lett. 180 (2000) 39–48.
[33] P. Burnard, D.W. Graham, G. Turner, Vesicle-specific noble gas analyses of "popping rock": implications for primordial noble gases in the Earth, Science 276 (1997) 568–571.
[34] A. Jambon, J.E. Shelby, Helium diffusion and solubility in obsidians and basaltic glass in the range 200–300 degrees C, Earth Planet. Sci. Lett. 51 (1980) 206–214.
[35] S. Niedermann, W. Bach, J. Erzinger, Noble gas evidence for a lower mantle component in MORBs from the Southern East Pacific Rise: decoupling of helium and neon isotope systematics, Geochim. Cosmochim. Acta 61 (1997) 2697–2715.
[36] J.E. Dixon, E. Stolper, J.R. Delaney, Infrared spectroscopic measurements of CO_2 and H_2O in Juan de Fuca Ridge basaltic glasses, Earth Planet. Sci. Lett. 90 (1988) 87–104.
[37] A.K. Shah, J.-C. Sempere, Morphology of the transition from an axial high to a rift valley at the Southeast Indian Ridge and the relation to variations in mantle temperature, J. Geophys. Res. 103 (1998) 5203–5223.
[38] C. Aubaud, F. Pineau, A. Jambon, M. Javoy, Kinetic disequilibrium of C, He, Ar and carbon isotopes during degassing of mid-ocean ridge basalts, Earth Planet. Sci. Lett. 222 (2004) 391–406.
[39] A.M. Shaw, D.R. Hilton, C.G. Macpherson, J.M. Stinton, The C–He–Ar systematics of the Manus back-arc basin: resolving source composition from degassing and contamination effects, Geochim. Cosmochim. Acta 68 (2004) 1837–1855.
[40] P. Cartigny, N. Jendrzejewski, F. Pineau, E. Petit, M. Javoy, Volatile (C, N, Ar) variability in MORB and the respective roles of mantle source heterogeneity and degassing; the case of the Southwest Indian Ridge, Earth Planet. Sci. Lett. 194 (2001) 241–257.
[41] K.P. Jochum, A.W. Hofmann, E. Ito, H.M. Seufert, W.M. White, K, U, and Th in mid-ocean ridge basalt glasses and heat production, K/U and K/Rb in the mantle, Nature 306 (1983) 431–436.
[42] M. Rehkamper, A.W. Hofmann, Recycled ocean crust and sediment in Indian Ocean MORB, Earth Planet. Sci. Lett. 147 (1997) 93–106.
[43] I. Vlastûlic, H. Bougalt, L. Dosso, Heterogeneous heat production in the Earth's upper mantle: blob melting and MORB composition, Earth Planet. Sci. Lett. 199 (2002) 157–172.
[44] B.J. Wood, J.D. Blundy, The effect of cation charge on crystal-melt partitioning of trace elements, Earth Planet. Sci. Lett. 188 (2001) 59–71.
[45] T. Torgersen, J. O'Donnell, The degassing flux from the solid Earth; release by fracturing, Geophys. Res. Lett. 18 (1991) 951–954.
[46] M. Honda, K. Kurita, Y. Hamano, M. Ozima, Experimental studies of He and Ar degassing during rock fracturing, Earth Planet. Sci. Lett. 59 (1982) 429–436.
[47] M. Jull, P.B. Kelemen, K. Sims, Consequences of diffuse and channeled porous melt migration on uranium series disequilibria, Geochim. Cosmochim. Acta 66 (2002) 4133–4148.
[48] D. McKenzie, Constraints on melt generation and transport from U-series activity ratios, Chem. Geol. 162 (2000) 81–94.
[49] P.B. Kelemen, M. Braun, G. Hirth, Spatial distribution of melt conduits in the mantle beneath oceanic spreading ridges: observations from the Ingalls and Oman ophiolites, Geochem. Geophys. Geosysts. 1 (2000) 1999GC000012.
[50] B.K. Holtzman, D.L. Kohlstedt, M.E. Zimmerman, F. Heidelbach, T. Hiraga, J. Hustoft, Melt segregation and strain partitioning: implications for seismic anisotropy and mantle flow, Science 301 (2003) 1227–1230.
[51] B.K. Holtzman, N.J. Groebner, M.E. Zimmerman, S.B. Ginsberg, D.L. Kohlstedt, Stress-driven melt segregation in partially molten rock, Geochem. Geophys. Geosysts. 4 (2003) DOI:10.1029/2001GC000258.
[52] S.R. Hart, Equilibration during mantle melting: a fractal tree model, Proc. Natl. Acad. Sci. U. S. A. 90 (1993) 11914–11918.
[53] T. Trull, M.D. Kurz, Experimental measurements of ^{3}He and ^{4}He mobility in olivine and clinopyroxene at magmatic temperatures, Geochim. Cosmochim. Acta 47 (1993) 1313–1324.
[54] M. Trieloff, J. Kunz, D.A. Clague, D. Harrison, C.J. Allûgre, The nature of pristine noble gases mantle plumes, Science 288 (2000) 1036–1038.
[55] M. Moreira, J. Kunz, C. Allûgre, Rare gas systematics in Popping Rock: isotopic and elemental compositions in the upper mantle, Science 279 (1998) 1178–1181.
[56] M. Honda, I. McDougall, Primordial helium and neon in the Earth; a speculation on early degassing, Geophys. Res. Lett. 25 (1998) 1951–1954.
[57] E. Anders, D. Heymann, E. Mazor, Isotopic composition of primordial helium in carbonaceous chondrites, Geochim. Cosmochim. Acta 34 (1970) 127–132.
[58] J.-P. Benkert, H. Baur, P. Signer, R. Wieler, He, Ne, and Ar from the solar wind and solar energetic particles in lunar ilmenites and pyroxenes, J. Geophys. Res., E 98 (1993) 13147–13162.
[59] I. Yatsevich, M. Honda, Production of nucleogenic neon in the Earth from natural radioactive decay, J. Geophys. Res. 102 (1997) 10291–10298.
[60] J.E. Dixon, E. Stolper, An experimental study of water and carbon dioxide solubilities in mid-ocean ridge basaltic liquids. Part II: applications to degassing, Contrib. Mineral. Petrol. 36 (1995) 1633–1646.
[61] R.E. Sours-Page, Magmatic processes at mid-ocean ridges; evidence from lavas and melt inclusions from the Southeast Indian Ridge, the Endeavour Segment of the Juan de Fuca Ridge, and the northern East Pacific Rise, Doctoral, Oregon State University, 2000.

Table 1. Locations and amounts of samples analyzed

Helium	Gms loaded	< 100micr	Segment	Depth (m)	Lat (°S)	Long(°E)	Na8
WW10-75-4	712.0	176.0	C15	2610	43.575	92.662	3.08
WW10-76-1/1	632.9	103.1	C15	2652.5	43.882	93.114	2.56
WW10-76-1/2	528.6	376.0	C15	2652.5	43.882	93.114	2.56
WW10-76-1/3	881.0	692.0	C15	2652.5	43.882	93.114	2.56
WW10-76-1/4	374.0	243.0	C15	2652.5	43.882	93.114	2.56
WW10-77-7	731.9	n.d.	C15	2795	44.117	93.773	2.62
WW10-78-2	795.7	n.d.	C14	2719	44.833	94.833	2.80
WW10-82-35/1	801.0	208.0	C14	3180	45.185	95.585	2.77
WW10-88-1	929.4	163.8	C13	2567.5	47.076	96.833	2.47
WW10-92-1	694.9	177.8	C13	2668	48.101	98.943	2.77
WW10-100-1	551.7	160.7	C12	2850	47.630	101.530	2.75
WW10-115-2	834.9	n.d.	C9	3696	49.229	105.868	3.02
WW10-116-1	927.0	131.0	C9/8	4835	48.873	106.494	n.d.
WW10-117-1	615.4	n.d.	C8	3520	48.348	107.145	2.90
WW10-117-1a	791.0	176.8	C8	3520	48.348	107.145	2.90
WW10-120-7	926.4	116.4	C8	2803.5	48.332	107.489	n.d.
WW10-118-1	815.1	n.d.	C8	2673	48.428	107.527	2.96
WW10-118-1	719.0	170.0	C8	2673	48.428	107.527	2.96
WW10-122-1	788.0	135.0	C8	3255	48.700	108.200	2.82
WW10-125-1	910.0	n.d.	C7	3440	49.450	109.105	2.75
WW10-126-1	697.0	181.7	C7	3240	49.527	109.484	3.25
WW10-130-1	840.4	n.d.	C6	3515	49.775	111.133	3.09
WW10-134-1	929.0	n.d.	C5	3620	50.295	112.490	2.74
WW10-134-1/2	702.5	132.5	C5	3620	50.295	112.490	2.74
ww10-135-8	748.8	138.8	C5	3748	50.307	112.593	2.82
WW10-138-1	737.7	148.0	C4	3820	50.187	112.855	2.69
WW10-144-4	687.3	129.8	C3	3997	50.007	115.212	3.01
ww10-145-1/1	839.7	213.9	C3	4610	49.273	116.717	3.59
WW10-146-1/1	746.3	196.9	C2	4755	49.505	117.182	3.25

Table 2. He, Ne, Ar and CO_2 compositions of Southeast Indian Ridge basaltic glasses

Sample	cr#	^{4}He	$^{3}He/^{4}He$	^{20}Ne	$^{21}Ne/^{22}Ne$	$^{20}Ne/^{22}Ne$	^{40}Ar	$^{40}Ar/^{36}Ar$	$^{40}Ar^{*}$	CO_2
		x10^{-6}	Ra	x10^{-12}			x10^{-6}		x10^{-6}	x10^{-3}
75-4	1	0.122± 0.005	7.30± 0.5	0.008± 0.001	b.d.	b.d.	0.0037± 0.0004	<3120	.003± min	0.47± 0.01
75-4	2	2.26± 0.09	8.54± 0.1	0.046± 0.004	0.036± 0.002	10.5± 0.6	0.057± 0.002	2826± 155	0.051± 0.002	7.32± 0.05
75-4	3	4.01± 0.16	8.89± 0.1	0.072± 0.006	0.036± 0.003	10.2± 0.9	0.092± 0.003	3115± 172	0.084± 0.003	8.8± 0.1
75-4	**tot**	**6.39± 0.18**	**8.73± 0.1**	**0.126± 0.007**			**0.153± 0.004**		**0.138± min**	**16.6± 0.2**
76-1/1	1	0.143± 0.003	8.94± 0.2	7.1± 0.8	b.d.	b.d.	0.0006± 0.0002	280± 150	0.0003± 0.0002	0.49± 0.04
76-1/1	2	0.62± 0.01	8.90± 0.1	10.8± 1.1	b.d.	b.d.	0.0021± 0.0004	497± 196	0.0008± 0.0004	1.8± 0.1
76-1/1	3	0.39± 0.01	9.32± 0.2	2.7± 0.3	b.d.	b.d.	0.0010± 0.0001	1663± 534	0.0008± 0.0001	1.00± 0.04
76-1/1	4	2.54± 0.05	9.07± 0.1	10.3± 1.3	b.d.	b.d.	0.007± 0.001	1167± 181	0.0054± 0.0009	5.7± 0.2
76-1/1	**tot**	**3.70± 0.05**	**9.07± 0.1**	**30.9± 1.9**			**0.011± 0.001**		**0.0073± 0.0010**	**8.9± 0.2**
76-1/2	1	2.56± 0.05	3.79± 4.1	35.4± 1.7	0.033± 0.002	10.3± 0.3	0.030± 0.001	616± 52	0.015± 0.001	9.0± 0.2
76-1/2	3	1.74± 0.03	8.47± 0.1	16.7± 0.8	0.036± 0.003	10.8± 0.3	0.015± 0.001	845± 75	0.010± 0.001	2.27± 0.03
76-1/2	**Tot**	**4.31± 0.06**	**5.69± 2.5**	**52.1± 1.9**			**0.045± 0.001**		**0.025± 0.001**	**11.2± 0.2**
76-1/3	1	0.57± 0.01	8.63± 0.2	15.7± 0.8	b.d.	b.d.	0.0098± 0.0004	454± 40	0.0034± 0.0004	1.9± 0.1
76-1/3	2	3.09± 0.06	8.34± 0.1	48.9± 2.4	0.032± 0.002	10.4± 0.3	0.048± 0.002	492± 41	0.019± 0.002	9.6± 0.1
76-1/3	3	2.43± 0.04	8.25± 0.1	38.4± 1.9	0.035± 0.002	10.3± 0.2	0.031± 0.001	589± 50	0.015± 0.001	4.35± 0.04
76-1/3	**tot**	**6.10± 0.07**	**8.33± 0.1**	**103.0± 3.1**			**0.089± 0.002**		**0.038± 0.002**	**15.9± 0.1**
76-1/4	1	0.058± 0.001	8.85± 0.2	5.5± 0.3	b.d.	b.d.	0.0014± 0.0001	328± 35	0.0001± 0.0001	0.21± 0.04
76-1/4	2	0.97± 0.02	8.66± 0.1	26.2± 1.3	b.d.	b.d.	0.018± 0.001	427± 36	0.006± 0.001	1.19± 0.04
76-1/4	**Tot**	**1.03± 0.02**	**8.67± 0.1**	**31.7± 1.3**			**0.019± 0.001**		**0.006± 0.001**	**1.4± 0.1**
77-7	1	0.015± 0.001	8.40± 0.7	20.9± 1.1	0.032± 0.003	10.7± 0.3	0.0084± 0.0003	286± 16	0.0004± min	0.2± 0.1
77-7	2	1.85± 0.08	9.01± 0.1	91.9± 4.8	0.031± 0.001	9.7± 0.2	0.160± 0.005	910± 41	0.108± 0.005	10.6± 0.4
77-7	3	1.59± 0.07	8.55± 0.1	256.6± 13.4	0.031± 0.001	10.0± 0.2	0.222± 0.007	401± 18	0.058± 0.007	6.0± 0.2
77-7	**tot**	**3.46± 0.10**	**8.79± 0.1**	**369.4± 14.3**			**0.390± 0.008**		**0.167± min**	**16.8± 0.4**
78-2	1	0.20± 0.01	8.37± 0.1	60.7± 3.2	0.031± 0.002	10.2± 0.2	0.045± 0.001	298± 13	0.002± min	1.26± 0.05
78-2	2	1.60± 0.07	8.18± 0.1	99.9± 5.2	0.032± 0.002	10.3± 0.2	0.140± 0.004	477± 21	0.053± 0.004	11.9± 0.4
78-2	3	1.59± 0.07	8.39± 0.1	33.9± 1.8	0.038± 0.002	10.7± 0.3	0.084± 0.002	1294± 58	0.065± 0.002	12.0± 0.4
78-2	4	1.98± 0.08	8.42± 0.1	40.5± 2.1	0.035± 0.002	10.5± 0.2	0.096± 0.003	1461± 65	0.076± 0.003	12.8± 0.4

78-2	**tot**	**5.37± 0.13**	**8.34± 0.1**	**235.1± 6.7**			**0.364± 0.006**		**0.196± min**	**37.9± 0.7**	
82-35/1	1	0.051± 0.001	7.71± 0.3	4.5± 0.2	b.d.	b.d.	0.0090± 0.0003	1760± 105	0.0075± 0.0003	0.3± 0.1	
82-35/1	2	0.61± 0.01	8.20± 0.03	7.7± 0.3	b.d.	b.d.	0.085± 0.003	10590± 762	0.082± 0.003	3.7± 0.1	
82-35/1	3	0.61± 0.01	8.23± 0.1	10.1± 0.4	b.d.	b.d.	0.084± 0.003	8367± 493	0.081± 0.003	4.1± 0.1	
82-35/1	4	0.94± 0.02	8.21± 0.05	13.3± 0.6	b.d.	b.d.	0.126± 0.004	10751± 612	0.123± 0.004	5.5± 0.1	
82-35/1	5	1.43± 0.03	7.93± 0.1	23.1± 0.8	0.041± 0.003	11.3± 0.5	0.190± 0.007	10005± 569	0.185± 0.007	8.6± 0.1	
82-35/1	6	1.87± 0.03	7.99± 0.1	16.4± 0.5	b.d.	b.d.	0.257± 0.009	16317± 990	0.252± 0.009	10.6± 0.9	
82-35/1	7	0.39± 0.01	7.95± 0.2	6.1± 0.3	0.039± 0.005	11.1± 1.0	0.049± 0.002	6538± 380	0.046± 0.002	3.2± 1.5	
82-35/1	**tot**	**5.91± 0.05**	**8.05± 0.03**	**81.2± 1.3**			**0.800± 0.013**		**0.777± 0.013**	**36.0± 1.7**	
88-1	1	0.170± 0.005	9.35± 0.2	13.2± 1.0	b.d.	b.d.	0.0245± 0.0002	1233± 61	0.0186± 0.0002	0.8± 0.2	
88-1	2	1.10± 0.03	9.21± 0.2	36.9± 3.2	0.034± 0.002	10.4± 0.6	0.145± 0.001	2219± 103	0.126± 0.001	4.6± 0.2	
88-1	3	1.62± 0.04	9.37± 0.3	58.7± 4.7	0.034± 0.002	10.5± 0.5	0.228± 0.002	2918± 135	0.205± 0.002	5.0± 0.1	
88-1	**tot**	**2.90± 0.05**	**9.31± 0.2**	**108.8± 5.8**			**0.397± 0.002**		**0.349± 0.002**	**10.4± 0.3**	
92-1	1	0.15± 0.01	7.94± 0.2	79.3± 4.1	0.030± 0.001	10.7± 0.2	0.0099± 0.0003	388± 19	0.0024± 0.0003	1.4± 0.1	
92-1	2	1.50± 0.06	8.53± 0.2	11.7± 0.6	0.042± 0.002	10.3± 0.3	0.028± 0.001	10485± 911	0.027± 0.001	15.0± 0.5	
92-1	3	1.10± 0.05	8.32± 0.1	111.8± 5.8	0.029± 0.001	9.4± 0.2	0.083± 0.002	371± 17	0.017± 0.002	8.4± 0.3	
92-1	4	0.056± 0.002	7.87± 0.4	44.6± 2.3	0.029± 0.002	10.1± 0.3	0.0108± 0.0003	299± 17	0.001± min	0.4± 0.1	
92-1	**tot**	**2.81± 0.08**	**8.40± 0.1**	**247.4± 7.6**			**0.131± 0.003**		**0.047± min**	**25.2± 0.6**	
100-1	1	0.210± 0.004	7.59± 0.1	11.6± 0.6	b.d.	b.d.	0.0065± 0.0002	597± 53	0.0033± 0.0002	1.3± 0.1	
100-1	2	2.34± 0.04	7.30± 0.1	162.0± 7.9	0.030± 0.001	9.9± 0.3	0.101± 0.004	506± 42	0.042± 0.004	18.1± 0.3	
100-1	3	1.20± 0.02	7.19± 0.1	76.6± 3.7	0.034± 0.002	10.1± 0.2	0.091± 0.003	1079± 89	0.066± 0.003	26.6± 0.4	
100-1	**Tot**	**3.74± 0.05**	**7.28± 0.1**	**250.3± 8.8**			**0.198± 0.005**		**0.111± 0.005**	**46.0± 0.5**	
115-2	1	0.151± 0.004	7.27± 0.2	23.9± 1.0	0.030± 0.002	10.0± 0.2	0.018± 0.001	563± 28	0.008± 0.001	1.5± 0.1	
115-2	2	1.07± 0.03	7.23± 0.1	91.2± 3.9	0.031± 0.001	10.0± 0.2	0.123± 0.004	829± 38	0.079± 0.004	11.7± 0.4	
115-2	3	1.16± 0.03	7.18± 0.1	47.3± 2.0	0.035± 0.002	10.3± 0.2	0.106± 0.003	1469± 67	0.085± 0.003	11.8± 0.4	
115-2	4	1.07± 0.03	7.26± 0.1	14.4± 0.6	0.043± 0.003	11.0± 0.2	0.061± 0.002	3961± 187	0.056± 0.002	8.4± 0.3	
115-2	**tot**	**3.44± 0.05**	**7.22± 0.1**	**176.8± 4.6**			**0.308± 0.005**		**0.229± 0.005**	**33.3± 0.6**	
116-15	1	0.65± 0.01	5.54± 2.5	6.9± 0.3	b.d.	b.d.	0.024± 0.001	18629± 3314	0.024± 0.001	17.0± 0.2	
116-15	2	0.42± 0.01	6.61± 0.2	67.9± 3.3	0.034± 0.002	10.2± 1.4	0.094± 0.003	630± 52	0.050± 0.003	34.5± 0.4	
116-15	3	1.10± 0.02	7.51± 0.1	27.3± 1.3	0.036± 0.002	10.1± 0.7	0.038± 0.001	1266± 109	0.029± 0.001	19.4± 0.2	
116-15	**Tot**	**2.17± 0.02**	**6.75± 0.7**	**102.1± 3.6**			**0.157± 0.004**		**0.103± 0.004**	**70.9± 0.5**	
117-1	1	0.42± 0.02	7.49± 0.1	12.0± 0.6	b.d.	10.3± 0.3	0.025± 0.001	7106± 589	0.024± 0.001	3.8± 0.2	
117-1	2	1.16± 0.05	7.47± 0.1	18.1± 0.9	0.034± 0.002	10.8± 0.3	0.082± 0.002	4560± 228	0.077± 0.002	12.3± 0.4	

117-1	3	1.52± 0.06	7.33± 0.1	20.0± 1.0	0.042± 0.002	11.0± 0.3	0.088± 0.003	3247± 157	0.080± 0.003	12.6± 0.4
117-1	4	0.20± 0.01	7.03± 0.4	187.6± 9.8	0.030± 0.001	9.8± 0.2	0.109± 0.003	263± 12	0.006± min	0.39± 0.04
117-1	**tot**	**3.31± 0.08**	**7.38± 0.1**	**237.7± 9.9**			**0.303± 0.005**		**0.186± min**	**29.0± 0.6**
117-1/1	1	0.150± 0.003	6.82± 0.3	2.9± 0.1	b.d.	b.d.	0.0071± 0.0003	6562± 1113	0.0067± 0.0003	1.96± 0.03
117-1/1	2	0.49± 0.01	6.59± 0.7	12.0± 0.6	b.d.	b.d.	0.086± 0.003	10989± 1022	0.084± 0.003	23.2± 0.2
117-1/1	3	1.75± 0.03	6.69± 0.1	18.6± 0.9	b.d.	b.d.	0.082± 0.003	8440± 761	0.079± 0.003	24.8± 0.2
117-1/1	4	1.57± 0.03	6.74± 0.1	15.7± 0.8	b.d.	b.d.	0.081± 0.003	7746± 694	0.078± 0.003	21.8± 0.2
117-1/1	5	1.48± 0.03	6.75± 0.1	13.8± 0.7	b.d.	b.d.	0.115± 0.004	10841± 1003	0.112± 0.004	16.0± 0.1
117-1/1	**Tot**	**5.44± 0.05**	**6.72± 0.1**	**63.0± 1.5**			**0.370± 0.006**		**0.359± 0.006**	**87.7± 0.3**
118-1	1	0.30± 0.01	7.27± 0.1	82.4± 4.8	0.030± 0.002	9.8± 0.2	0.042± 0.001	310± 15	0.002± 0.001	1.7± 0.1
118-1	2	2.16± 0.06	7.39± 0.1	225.0± 13.2	0.031± 0.002	10.1± 0.2	0.139± 0.004	339± 16	0.018± 0.004	11.8± 0.4
118-1	3	0.64± 0.02	7.39± 0.1	99.1± 5.8	0.030± 0.002	10.1± 0.2	0.055± 0.002	318± 16	0.004± 0.002	1.0± 0.1
118-1	**tot**	**3.10± 0.06**	**7.38± 0.1**	**406.5± 15.3**			**0.236± 0.005**		**0.024± 0.005**	**14.5± 0.4**
118-1/2	1	0.115± 0.002	7.09± 0.2	15.3± 0.7	b.d.	b.d.	0.0082± 0.0003	332± 29	0.0009± 0.0003	2.2± 0.2
118-1/2	2	1.28± 0.02	6.70± 0.1	114.7± 5.6	0.030± 0.001	9.9± 0.2	0.069± 0.002	362± 30	0.013± 0.002	11.6± 0.4
118-1/2	3	0.71± 0.01	6.71± 0.1	60.5± 2.9	0.031± 0.002	10.1± 0.3	0.035± 0.001	349± 29	0.005± 0.001	2.6± 0.1
118-1/2	**Tot**	**2.11± 0.03**	**6.72± 0.1**	**190.5± 6.4**			**0.112± 0.003**		**0.019± 0.003**	**16.4± 0.4**
120-7	1	0.176± 0.003	6.93± 0.2	21.7± 1.1	b.d.	b.d.	0.016± 0.001	368± 31	0.003± 0.001	2.3± 0.3
120-7	2	1.51± 0.03	6.62± 0.1	128.9± 6.3	0.030± 0.001	10.1± 0.3	0.089± 0.003	439± 36	0.029± 0.003	18.0± 0.5
120-7	3	1.89± 0.03	6.56± 0.1	33.2± 1.6	0.038± 0.002	10.9± 0.3	0.054± 0.002	1010± 85	0.038± 0.002	19.1± 0.3
120-7	**tot**	**3.57± 0.04**	**6.61± 0.1**	**183.8± 6.6**			**0.159± 0.004**		**0.070± 0.004**	**39.4± 0.6**
122-1	1	0.035± 0.001	6.91± 0.3	7.6± 0.4	b.d.	b.d.	0.0032± 0.0001	405± 40	0.0009± 0.0001	0.33± 0.02
122-1	2	1.53± 0.03	6.66± 0.1	61.4± 3.0	0.034± 0.002	10.1± 0.2	0.097± 0.003	1091± 91	0.071± 0.003	17.5± 0.1
122-1	3	0.43± 0.01	6.59± 0.2	52.9± 2.6	0.031± 0.002	10.0± 0.3	0.037± 0.001	419± 35	0.011± 0.001	0.8± 0.0
122-1	**Tot**	**2.00± 0.03**	**6.65± 0.1**	**121.9± 4.0**			**0.138± 0.004**		**0.083± 0.004**	**18.7± 0.1**
125-1	1	0.107± 0.005	7.52± 0.2	10.2± 0.5	b.d.	b.d.	0.0071± 0.0002	726± 34	0.0042± 0.0002	0.9± 0.1
125-1	2	1.14± 0.05	7.41± 0.2	108.3± 5.7	0.030± 0.001	10.0± 0.3	0.113± 0.003	676± 30	0.064± 0.003	10.7± 0.4
125-1	3	1.36± 0.06	7.52± 0.1	33.8± 1.8	0.033± 0.002	9.9± 0.2	0.095± 0.003	1679± 74	0.079± 0.003	12.7± 0.4
125-1	4	1.45± 0.06	7.56± 0.1	73.8± 3.9	0.033± 0.001	10.2± 0.3	0.113± 0.003	1086± 48	0.082± 0.003	13.1± 0.5
125-1	5	1.91± 0.08	7.42± 0.1	68.3± 3.6	0.035± 0.002	10.2± 0.2	0.110± 0.003	2229± 103	0.096± 0.003	16.1± 0.5
125-1	6	2.23± 0.09	7.07± 0.1	63.3± 3.3	0.034± 0.002	10.3± 0.2	0.160± 0.005	1783± 79	0.134± 0.005	21.1± 0.7
125-1	**tot**	**8.20± 0.16**	**7.37± 0.1**	**357.7± 8.6**			**0.599± 0.008**		**0.458± 0.008**	**74.6± 1.1**
126-1	1	0.04± 0.02	7.56± 3.3	31.3± 1.5	b.d.	b.d.	0.018± 0.001	305± 26	0.001± 0.001	0.5± 0.6

126-1	2	0.67± 0.01	6.94± 0.2	69.7± 3.4	0.031± 0.001	9.9± 1.3	0.047± 0.002	420± 35	0.014± 0.002	29.8± 0.2
126-1	3	0.55± 0.01	6.97± 0.6	65.1± 3.2	0.031± 0.001	10.1± 3.4	0.041± 0.001	426± 35	0.013± 0.001	25.8± 0.2
126-1	4	0.44± 0.01	5.64± 3.1	10.1± 0.5	b.d.	b.d.	0.0049± 0.0002	483± 43	0.0019± 0.0002	1.03± 0.03
126-1	**Tot**	**1.69± 0.02**	**6.62± 0.8**	**176.3± 4.9**			**0.111± 0.002**		**0.029± 0.002**	**57.1± 0.7**
130-1	1	0.033± 0.001	6.96± 0.3	11.6± 0.6	b.d.	b.d.	0.0080± 0.0003	717± 35	0.0047± 0.0003	0.24± 0.02
130-1	2	1.84± 0.08	7.74± 0.1	47.0± 2.5	0.038± 0.002	10.7± 0.2	0.365± 0.011	4504± 200	0.341± 0.011	14.9± 0.5
130-1	3	0.96± 0.04	7.49± 0.2	23.8± 1.2	0.038± 0.002	10.5± 0.2	0.200± 0.006	10135± 492	0.194± 0.006	5.7± 0.2
130-1	**tot**	**2.83± 0.09**	**7.65± 0.1**	**82.4± 2.8**			**0.573± 0.012**		**0.540± 0.012**	**20.8± 0.5**
134-1	1	0.079± 0.003	7.70± 0.3	12.7± 0.7	0.036± 0.003	10.4± 0.3	0.0137± 0.0005	1978± 165	0.0116± 0.0005	0.6± 0.1
134-1	2	1.64± 0.07	7.68± 0.2	150.0± 7.8	0.032± 0.001	10.1± 0.2	0.359± 0.011	1307± 57	0.278± 0.011	16.8± 0.6
134-1	3	3.32± 0.14	7.40± 0.1	103.0± 5.4	0.039± 0.002	10.7± 0.3	0.601± 0.018	2770± 125	0.537± 0.018	36.4± 1.2
134-1	4	1.46± 0.06	7.70± 0.1	63.3± 3.3	0.034± 0.001	10.4± 0.2	0.276± 0.008	2073± 94	0.237± 0.008	14.0± 0.5
134-1	5	2.74± 0.12	7.47± 0.2	293.8± 15.4	0.032± 0.001	10.2± 0.2	0.601± 0.018	891± 40	0.402± 0.018	24.4± 0.8
134-1	**tot**	**9.24± 0.20**	**7.52± 0.1**	**622.8± 18.4**			**1.851± 0.029**		**1.465± 0.029**	**92.3± 1.7**
134-1/2	1	1.09± 0.02	7.28± 0.1	181.0± 8.8	0.027± 0.001	9.9± 2.1	0.253± 0.009	852± 71	0.165± 0.009	13.2± 0.1
134-1/2	**tot**	**1.09± 0.02**	**7.28± 0.1**	**181.0± 8.8**			**0.253± 0.009**		**0.165± 0.009**	**13.2± 0.1**
135-8	1	0.080± 0.001	7.34± 0.3	6.8± 0.5	b.d.	b.d.	0.0127± 0.0002	2495± 316	0.0112± 0.0002	0.76± 0.02
135-8	2	1.28± 0.01	7.01± 0.2	68.6± 4.5	0.033± 0.002	9.9± 0.5	0.206± 0.002	1661± 133	0.169± 0.002	10.60± 0.04
135-8	3	1.72± 0.02	7.06± 0.2	15.3± 1.1	0.050± 0.004	10.4± 0.6	0.227± 0.002	16502± 1838	0.223± 0.002	14.06± 0.04
135-8	4	2.10± 0.02	7.14± 0.2	17.8± 1.3	0.053± 0.005	11.5± 0.8	0.278± 0.002	20192± 1925	0.274± 0.002	16.8± 0.1
135-8	5	1.53± 0.02	7.16± 0.2	12.4± 0.9	0.050± 0.006	11.3± 0.9	0.184± 0.002	16022± 1686	0.180± 0.002	8.77± 0.03
135-8	**tot**	**6.70± 0.04**	**7.10± 0.1**	**120.9± 4.9**			**0.907± 0.004**		**0.858± 0.004**	**51.0± 0.1**
138-1	1	0.48± 0.02	8.19± 0.1	4.4± 0.2	0.038± 0.004	9.6± 0.3	0.034± 0.001	7469± 591	0.032± 0.001	2.7± 0.1
138-1	2	2.07± 0.09	7.60± 0.1	14.0± 0.7	0.048± 0.004	11.0± 0.3	0.181± 0.005	9609± 512	0.176± 0.005	12.8± 0.4
138-1	3	2.17± 0.09	8.00± 0.2	17.7± 0.9	0.057± 0.004	11.8± 0.3	0.206± 0.006	10520± 614	0.200± 0.006	13.2± 0.4
138-1	4	2.60± 0.11	7.78± 0.1	80.4± 4.2	0.034± 0.002	10.4± 0.2	0.213± 0.006	1507± 66	0.171± 0.006	9.8± 0.3
138-1	**TOT**	**7.32± 0.17**	**7.82± 0.1**	**116.6± 4.4**			**0.633± 0.010**		**0.579± 0.010**	**38.5± 0.7**
144-4	1	0.68± 0.01	6.98± 0.3	61.8± 4.9	0.031± 0.002	9.9± 0.7	0.095± 0.001	946± 25	0.065± 0.001	6.4± 0.2
144-4	2	1.33± 0.02	6.99± 0.5	54.1± 5.5	0.032± 0.003	9.9± 0.5	0.144± 0.001	1370± 38	0.113± 0.001	11.3± 0.3
144-4	3	1.15± 0.03	6.60± 0.2	12.3± 1.3	0.043± 0.004	9.4± 1.1	0.091± 0.001	7361± 411	0.087± 0.001	8.6± 0.3
144-4	4	1.98± 0.05	6.83± 0.1	79.6± 6.4	0.034± 0.002	10.3± 0.5	0.203± 0.002	1497± 68	0.163± 0.002	13.0± 0.4
144-4	**tot**	**5.15± 0.06**	**6.84± 0.1**	**207.8± 9.9**			**0.534± 0.002**		**0.429± 0.002**	**39.3± 0.6**
145-1/1	1	2.12± 0.04	6.75± 0.1	211.0± 21.8	0.029± 0.002	9.5± 1.2	0.059± 0.007	619± 216	0.031± 0.007	20.3± 0.6

145-1/1	2	2.05± 0.04	6.46± 0.1	106.4± 11.1	0.032± 0.004	9.5± 1.5	0.045± 0.005	824± 237	0.029± 0.005	19.1± 0.6
145-1/1	3	2.17± 0.04	6.66± 0.1	67.1± 6.9	0.035± 0.003	10.8± 1.3	0.038± 0.005	1069± 292	0.027± 0.005	18.4± 0.6
145-1/1	4	1.67± 0.03	6.55± 0.2	25.1± 2.6	0.037± 0.003	10.0± 1.2	0.027± 0.003	1445± 323	0.021± 0.003	11.3± 0.3
145-1/1	**tot**	**8.02± 0.07**	**6.61± 0.1**	**409.6± 25.5**			**0.167± 0.010**		**0.108± 0.010**	**69.0± 1.1**
146-1/1	1	0.345± 0.004	6.50± 0.2	8.2± 0.9	b.d.	b.d.	0.0530± 0.0005	4239± 218	0.0493± 0.0005	3.99± 0.03
146-1/1	2	0.82± 0.01	6.49± 0.1	14.7± 1.4	b.d.	b.d.	0.125± 0.001	4467± 204	0.117± 0.001	9.06± 0.02
146-1/1	3	0.54± 0.01	6.82± 0.2	14.9± 1.2	b.d.	b.d.	0.066± 0.001	2054± 92	0.056± 0.001	1.9± 0.1
146-1/1	**tot**	**1.71± 0.01**	**6.60± 0.1**	**37.8± 2.1**			**0.244± 0.001**		**0.222± 0.001**	**15.0± 0.1**

All abundances in cc STP (not per gram of sample; see Table 1 for sample weights). min = for samples with $^{40}Ar/^{36}Ar$ within error of the atmospheric ratio, the minimum possible $^{40}Ar^*$ has been calculated; b.d. = below detection.